The Astrophysical Journal, 739:93 (19pp), 2011 October 1 doi:10.1088/0004-637X/739/2/93

TYPE Ia SUPERNOVAE AS SITES OF THE *p*-PROCESS: TWO-DIMENSIONAL MODELS COUPLED TO NUCLEOSYNTHESIS

C. Travaglio[1,2], F. K. Röpke[3,4], R. Gallino[1,2,5], and W. Hillebrandt[4]
[1] INAF-Astronomical Observatory Teramo, Via Mentore Maggini snc, Loc. Collurania, 64100 Teramo, Italy; travaglio@oato.inaf.it, claudia.travaglio@b2fh.org
[2] B2FH Association-c/o Strada Osservatorio 20, 10023 Turin, Italy
[3] Universität Würzburg, Am Hubland, D-97074 Würzburg, Germany; fritz@mpa-garching.mpg.de
[4] Max-Planck-Institut für Astrophysik, Karl-Schwarzschild-Str. 1, D-85748 Garching bei München, Germany
[5] Dipartimento di Fisica Generale, Universitá di Torino, Via Pietro Giuria 1, 10125 Turin, Italy

Received 2011 March 11; accepted 2011 June 3; published 2011 September 14

ABSTRACT

Beyond Fe, there is a class of 35 proton-rich nuclides, between ^{74}Se and ^{196}Hg, called *p*-nuclei. They are bypassed by the *s* and *r* neutron capture processes and are typically 10–1000 times less abundant than the *s*- and/or *r*-isotopes in the solar system. The bulk of *p*-isotopes is created in the "gamma processes" by sequences of photodisintegrations and beta decays in explosive conditions in both core collapse supernovae (SNe II) and in Type Ia supernovae (SNe Ia). SNe II contribute to the production of *p*-nuclei through explosive neon and oxygen burning. However, the major problem in SN II ejecta is a general underproduction of the light *p*-nuclei for $A < 120$. We explore SNe Ia as *p*-process sites in the framework of a two-dimensional SN Ia delayed detonation model as well as pure deflagration models. The white dwarf precursor is assumed to have reached the Chandrasekhar mass in a binary system by mass accretion from a giant/main-sequence companion. We use enhanced *s*-seed distributions, with seeds directly obtained from a sequence of thermal pulse instabilities both in the asymptotic giant branch phase and in the accreted material. We apply the tracer-particle method to reconstruct the nucleosynthesis by the thermal histories of Lagrangian particles, passively advected in the hydrodynamic calculations. For each particle, we follow the explosive nucleosynthesis with a detailed nuclear reaction network for all isotopes up to ^{209}Bi. We select tracers within the typical temperature range for *p*-process production, $(1.5–3.7) \times 10^9$ K, and analyze in detail their behavior, exploring the influence of different *s*-process distributions on the *p*-process nucleosynthesis. In addition, we discuss the sensitivity of *p*-process production to parameters of the explosion mechanism, taking into account the consequences on Fe and alpha elements. We find that SNe Ia can produce a large amount of *p*-nuclei, both the light *p*-nuclei below $A = 120$ and the heavy-*p* nuclei, at quite flat average production factors, tightly related to the *s*-process seed distribution. For the first time, we find a stellar source able to produce both light and heavy *p*-nuclei almost at the same level as ^{56}Fe, including the debated neutron magic ^{92,94}Mo and ^{96,98}Ru. We also find that there is an important contribution from the *p*-process nucleosynthesis to the *s*-only nuclei ^{80}Kr, ^{86}Sr, to the neutron magic ^{90}Zr, and to the neutron-rich ^{96}Zr. Finally, we investigate the metallicity effect on *p*-process production in our models. Starting with different *s*-process seed distributions for two metallicities $Z = 0.02$ and $Z = 0.001$, running two-dimensional SN Ia models with different initial composition, we estimate that SNe Ia can contribute to at least 50% of the solar *p*-process composition. A more detailed analysis of the role of SNe Ia in Galactic chemical evolution of *p*-nuclei is in preparation.

Key words: hydrodynamics – nuclear reactions, nucleosynthesis, abundances – supernovae: general

Online-only material: color figures

1. INTRODUCTION

Among the nuclei heavier than ^{56}Fe, there is a class of 35 nuclides called *p*-nuclei, which are typically 10–1000 times less abundant than the *s*- or *r*-isotopes in the solar system. They cannot be synthesized by neutron-capture processes since they are located on the neutron-deficient side of the valley of β-stability. The astrophysical origin of *p*-nuclei has been studied for 50 years, starting from the pioneering works by Cameron (1957) and Burbidge et al. (1957). They suggested that a combination of proton captures and photodissociations of *s*- and *r*-seed nuclei could produce *p*-nuclei at temperatures between 2 and 3×10^9 K. About 20 years later, different attempts were made to explain the synthesis of all *p*-nuclei in one astrophysical site (Audouze & Truran 1975; Arnould 1976; Woosley & Howard 1978). Those authors suggested that the largest fraction of *p*-isotopes in the solar system should be created by photodisintegration (the so-called γ-process) reactions operating upon a distribution of *s*-process seeds synthesized in the earlier evolutionary stages of the progenitor. They suggested Type II supernovae (hereafter SNe II) as the astrophysical site of the *p*-process and demonstrated that the *p*-process is extremely sensitive to temperature and timescales. Detailed calculations of *p*-process nucleosynthesis in SNe II have been performed by many authors, e.g., Woosley & Howard (1990), Rayet et al. (1990, 1995), Rauscher et al. (2002), Hayakawa et al. (2006, 2008), and Farouqi et al. (2009). In these studies, core-collapse supernovae have been considered the best candidates for reproducing the solar abundances of the bulk of the *p*-isotopes. However, it has been shown that the "gamma-process" scenario suffers from a strong underproduction of the most abundant *p*-isotopes, ^{92,94}Mo (see, e.g., Fisker et al. 2009) and ^{96,98}Ru. For these nuclei, alternative processes and sites have been proposed, either strong neutrino fluxes in the deepest layers of SN II ejecta (Frölich et al. 2006), or rapid proton-captures in proton-rich, hot matter accreted onto the surface of a neutron star (e.g., Schatz et al. 2001), with the νp-process in neutrino-driven winds of SNe II (e.g., Frölich et al. 2006; Pruet et al. 2006; Wanajo 2006; Wanajo et al. 2011a, 2011b). Woosley et al. (1990) additionally introduced a ν-process to reproduce ^{138}La and ^{180m}Ta. Recent multidimensional SN II models show that the ejecta can become proton-rich for several seconds (Fisher et al. 2010), and the importance of the nucleosynthesis (including the νp-process) in the reverse shock has been studied in detail (Wanajo et al. 2011a; Roberts et al. 2010; Arcones & Janka 2011). Fujimoto et al. (2007) performed calculations of the composition of magnetically driven jets ejected from a collapsar, based on magnetohydrodynamic simulations of a rapidly rotating massive star during core collapse. They found that not only does the *r*-process successfully operate in the jets (with a pattern inside the jets similar to that of the *r*-elements in the solar system), but also *p*-nuclei are produced without the need of *s*-seeds. Light *p*-nuclei, such as ^{74}Se, ^{78}Kr, ^{84}Sr, and ^{92}Mo, are abundantly synthesized in the jets, together with ^{113}In, ^{115}Sn, and ^{138}La. They claim that the amounts of *p*-nuclei in the ejecta are much larger than those in core-collapse supernovae. More recently, a different possibility for synthesizing light *p*-nuclei has been presented by Wanajo et al. (2011a) and Arcones & Montes (2011). These authors explored the possibility of synthesis of *p*-nuclei in proton-rich winds of SNe II. Other possible scenarios for the production of *p*-nuclei have been proposed by Iwamoto et al. (2005) considering hypernovae, by Fujimoto et al. (2003) suggesting accretion disks around compact objects, and by Nishimura et al. (2006) investigating jet-like explosions.

The *p*-process has also been suggested to occur in the outermost layers of Type Ia supernovae (SNe Ia), based on a delayed detonation model (Howard & Meyer 1993), He-detonation models for a sub-Chandrasekhar mass white dwarf (WD; Goriely et al. 2005; Arnould & Goriely 2006), and by Kusakabe et al. (2005, 2011) based on the W7 carbon deflagration model (Nomoto et al. 1984). All these authors considered both solar abundances as seeds for the *p*-process and *s*-enhanced seeds. Goriely et al. (2002), presenting one-dimensional He-detonating, sub-Chandrasekhar mass carbon–oxygen white dwarf models (hereafter CO-WD), and Goriely et al. (2005), presenting three-dimensional explosion models, concluded that sub-Chandrasekhar He-detonation models are not an efficient site for the synthesis of *p*-nuclei.

Kusakabe et al. (2005, 2011) analyzed the effects of different *s*-seed distributions on *p*-production. They derived the *s*-seed distribution by assuming an exponential distribution of neutron exposures with two choices of the mean exposure $\tau_0 = 0.30$ mb^{-1}, which best reproduces the main component in the solar system (Arlandini et al. 1999, the classical model), or $\tau_0 = 0.15$ mb^{-1}, which gives rise to an *s*-process distribution decreasing with increasing atomic mass number *A*. The accuracy of the treatment of the outer zones of the SN Ia is fundamental for *p*-nuclei production, and the sparse zoning in the outermost layers of the W7 model has to be taken into account for thorough *p*-process nucleosynthesis calculations. As we will describe in this paper, our multidimensional SN Ia models can follow quite accurately even the outermost parts of the star.

We have calculated *p*-process nucleosynthesis with high-resolution two-dimensional hydrodynamic models of SNe Ia considering both a pure deflagration (similar to Röpke et al. 2006) and delayed detonations of different explosion strengths (similar to those presented in Kasen et al. 2009). We also have calculated *p*-process nucleosynthesis for SNe Ia of metallicity lower than solar. The adopted SN Ia models are detailed in Section 2. The tracer particle method of calculating the nucleosynthesis in multidimensional simulations (see, e.g., Travaglio et al. 2004; Maeda et al. 2010), together with the nuclear reaction network, is described in Section 3. We consider different *s*-process seed distributions, as detailed in Section 4. In Section 5, we show an analysis of the production mechanisms of all *p*-nuclei. The results for the *p*-process production, depending on the different SN Ia models adopted and on the *s*-process distribution tested, are discussed in Section 6. Finally, conclusions and work in progress are described in Section 7.

2. TYPE Ia SUPERNOVA MODELS

SNe Ia are associated with thermonuclear explosions of WD stars that are composed of carbon and oxygen. A favored scenario is that the explosion is triggered once the WD approaches the Chandrasekhar mass. In the *single-degenerate scenario* to which we refer here, this happens due to accretion of material from a main-sequence or evolved companion star in a binary system. We follow the explosion phase of Chandrasekhar-mass WD in two-dimensional hydrodynamic simulations. The numerical method employed has been described in detail by Reinecke et al. (1999), Röpke & Niemeyer (2007), Röpke & Schmidt (2009), and Röpke (2005).

For the explosion, a number of scenarios have been suggested (see Hillebrandt & Niemeyer 2000 for a review). Here, we focus on pure deflagrations and delayed detonations. In the former, the burning front propagates subsonically throughout the explosion. It is subject to instabilities that drive turbulence due to which the flame is strongly accelerated beyond its laminar burning speed. However, the pure deflagration model is not considered a candidate for most of the normal SNe Ia as it falls short of reproducing the necessary explosion energies and ^{56}Ni masses (Röpke et al. 2007), although it may be an explanation for the peculiar sub-class of 2002cx-like SNe Ia (Phillips et al. 2007). A transition of the flame propagation mode from subsonic deflagration to supersonic detonation in a late stage of the burning constitutes the delayed detonation model (Khokhlov 1991). The necessary deflagration-to-detonation transition (DDT) may arise from strong turbulence in the so-called distributed burning regime (e.g., Röpke 2007; Woosley 2007; Woosley et al. 2009), but rigorous evidence for its occurrence in SNe Ia is still lacking and details of its physical mechanism are uncertain. Nonetheless, delayed detonations successfully reproduce main observables of normal SNe Ia (Mazzali et al. 2007; Kasen et al. 2009) and are therefore considered a standard model for these events.

Our hydrodynamic simulations do not follow the evolution of the WD toward ignition, but start at the onset of the explosion. Here, we ignite a cold ($T = 5.0 \times 10^5$ K) Chandrasekhar-mass WD in hydrostatic equilibrium with a chemical composition that results from three different evolutionary phases of the progenitor, i.e., central He-burning, He-shell burning during the early asymptotic giant branch (AGB) phase, and He-shell burning during the thermally pulsing AGB phase (Domínguez et al. 2001). According to Piro & Bildsten (2008) and Jackson et al. (2010), we assume that as soon as the accreting WD approaches the Chandrasekhar, mass carbon-burning starts to occur in the core. The energy released by this burning drives convection (the so-called *simmering phase*) that lasts for about 1000 years before the explosion. The extension of this convective zone is not well determined, and the most external zones beyond 1.2 $M_\odot$

Table 1
Results of the Hydrodynamic SN Ia Explosion Simulations: Asymptotic Kinetic Energy $E_{\text{kin}}^{\text{asym}}$ and Final Composition (Iron Group Elements: IGEs, Intermediate-mass Elements: IMEs)

Model	$E_{\text{kin}}^{\text{asym}}$ (10^{51} erg)	M(IGEs)	M(IMEs)	M(C)	M(O)
DEF-a	0.3522	0.497	0.081	0.357	0.472
DDT-a	1.3027	0.767	0.509	0.018	0.113
DDT-b	1.2903	0.759	0.522	0.018	0.114
DDTw-a	1.1142	0.531	0.644	0.046	0.187
DDTs-a	1.5017	1.142	0.215	0.007	0.044

Note. All masses are given in solar masses $M_{\odot}$.

may well remain unmixed (Piro & Bildsten 2008). Note that the zone where the bulk of the p-isotopes is produced is the most external one, with an extension of the order of $\sim 0.1\, M_{\odot}$.

For our DDT-a model, we use a CO-WD structure presented by Domínguez et al. (2001) (Table 1), with $Z = 0.02$ and a progenitor mass of $M = 1.5\, M_{\odot}$. The sensitivity to the different CO-WD structure (obtained evolving models with different main-sequence mass) and the uncertainties in the extension of the simmering phase suggest that a uniform C/O ratio with 50% mixture for the burning can be a good approximation. Concerning the initial Y_e, two different setups are used; the first one, marked with **a**, assumes $Y_e = 0.499$, i.e., close to solar metallicity[6] $Z_{\odot}$. Setup **b** assumes $Y_e = 0.4995$ (corresponding to $\sim 1/20\, Z_{\odot}$). All simulations were performed with 512×1024 non-uniform moving computational grid cells adopting the nested-grid technique of Röpke & Hillebrandt (2005).

In all models discussed in this paper, the thermonuclear burning front is ignited in multiple sparks (Röpke et al. 2006) near the center of the WD. Specifically, we chose the setup of model DD2D_iso_05 of Kasen et al. (2009; 90 ignition kernels of 6 km radius randomly placed in the radial direction according to a Gaussian distribution with a width of 150 km) for all but one model, where we employ the ignition kernel distribution of model DD2D_iso_01 (20 ignition kernels of the same radius placed according to a Gaussian radial distribution with a standard deviation of 150 km).

The chosen WD setups and the explosion scenarios considered result in the following five different hydrodynamic explosion models.

1. *DEF-a*. A pure deflagration model assuming the WD setup **a**.
2. *DDT-a*. A delayed detonation model assuming the WD setup **a** and the deflagration-to-detonation criterion dc2 of Kasen et al. (2009). Detonations are triggered at any point on the deflagration flame where a Karlovitz number of Ka = 250 is reached while the fuel density is in the range $0.6 \lesssim \rho_{\text{fuel}}/(10^7\,\text{g cm}^{-3}) \lesssim 1.2$.
3. *DDT-b*. A delayed detonation model assuming the WD setup **b** and the same deflagration-to-detonation criterion dc2 of Kasen et al. (2009).
4. *DDTw-a*. A delayed detonation model assuming the WD setup **a** and the deflagration-to-detonation criterion dc4 of Kasen et al. (2009), i.e., detonations are this time triggered at any point on the deflagration flame where a Karlovitz number of Ka = 1500 is reached while the fuel density is in the range $0.6 \lesssim \rho_{\text{fuel}}/(10^7\,\text{g cm}^{-3}) \lesssim 1.2$.
5. *DDTs-a*. A delayed detonation model assuming the WD setup **a**, the ignition kernel distribution DD2D_iso_01, and the deflagration-to-detonation criterion dc2 of Kasen et al. (2009).

The results of the hydrodynamic explosion simulations are summarized in Table 1. Those of the delayed detonation models are not identical to (but are reasonably close to) the results of the corresponding models presented in Kasen et al. (2009) where different initial WD models were used. The pure-deflagration model produces little ^{56}Ni and the explosion energy is particularly low because—as is characteristic for pure deflagration models—burning ceases quickly after nuclear statistical equilibrium (NSE) is no longer reached in the ashes, and only about a tenth of a solar mass of intermediate-mass elements is produced. More than half of the WD mass remains unburned. Since the iron group nuclei are synthesized at rather high densities, neutronization is efficient and a large fraction of the iron group nuclei are Fe and Ni stable isotopes rather than ^{56}Ni. As expected, the DD2D_iso_05 ignition kernel setup in combination with the dc2 DDT criterion leads to an explosion strength ($E_{\text{kin}}^{\text{asym}} \sim 1.3 \times 10^{51}$ erg) and a ^{56}Ni mass ($\sim 0.5\, M_{\odot}$) that are typical for "normal" SNe Ia, and the effect of the two WD models (**a** versus **b**) is of secondary importance for the global explosion characteristics. The two additional models, DDTw-a and DDTs-a, were computed to explore the range of explosion strengths that is observed for normal SNe Ia. With ^{56}Ni masses of $0.301\, M_{\odot}$ and $0.951\, M_{\odot}$ they capture the extreme limits of the range (or perhaps even exceed them slightly).

The multidimensional SN Ia simulations described above assume instant burning of the initial C+O material once crossed by a deflagration or detonation front (which is represented as a discontinuity applying the level-set method). The microphysical details of the burning are not resolved. Instead, the fuel material is converted to an ash composition according to the fuel density ahead of the front. The ash material is modeled by a mixture of ^{56}Ni and α-particles representing NSE that is dynamically adjusted according to the thermodynamic conditions during the simulation and by a hypothetical (but representative) intermediate-mass nucleus ($A = 30$, $E_{\text{bind}} = 6.8266 \times 10^{18}\,\text{erg g}^{-1}$). At the lowest fuel densities above the burning threshold, burning from carbon to oxygen (which also mimics burning to neon) is included. The neutronization of the material is treated independently of this composition by advecting Y_e as a passive scalar and taking into account its evolution due to electron capture reactions in the NSE material. This coarse treatment of nuclear reactions is sufficient to account with sufficient precision for the energy release that drives the explosion dynamics. A more detailed treatment, however, is necessary to analyze the specific nucleosynthetic processes that are the focus of our present work. To this end, a number of Lagrangian tracer particles that record thermodynamic trajectories are passively advected with the hydrodynamic flow in the explosion simulation. On that basis, a post-processing step is performed using an extended network up to ^{209}Bi as described in the following section. The masses of the species in the ejecta quoted above (and shown in Table 1) are therefore only an estimate. More reliable values are obtained in the nucleosynthetic postprocessing step.

3. NUCLEOSYNTHESIS IN MULTIDIMENSIONAL SNe Ia

The multidimensional hydrodynamic scheme we use follows the explosion by means of an Eulerian grid. In order to

---

[6] Note that in our hydrodynamic simulations, Y_e is treated as an independent parameter and does not reflect the actual chemical composition of the WD material as modeled here.

Table 2
SN Ia Models: Main Species

Species	DDT-a	DDT-b	DEF-a	DDTw-a	DDTs-a	W7[a]
^{56}Fe	0.583	0.487	0.317	0.301	0.986	0.669
^{12}C	0.016	0.017	0.354	0.035	0.002	0.050
^{16}O	0.144	0.152	0.538	0.39	0.030	0.140
$\triangle M_p$[b]	0.130	0.114	0.090	0.380	0.06	

Notes.
[a] Iwamoto et al. (1999).
[b] Fraction of the mass of the star (in $M_\odot$) where p-process nucleosynthesis occurs for the SN Ia models presented in this work.

follow over time the temperature and density evolution of the fluid, we introduce a Lagrangian component in the form of tracer particles. During the hydrodynamic simulation, they are advected by the flow, recording the T and ρ history along their paths. The nuclear post-processing calculations are then performed separately for each particle. The tracer particle method for nucleosynthesis calculations for core-collapse SNe was first introduced by Nagataki et al. (1997), and for SNe Ia by Travaglio et al. (2004, 2005).

For the present work we use 51,200 tracer particles, uniformly distributed in mass coordinate. Each tracer represents the same mass of $\simeq 2.73 \times 10^{-5}\ M_\odot$ ($= M_{\rm WD}/51{,}200$). The distribution of the tracer particles for our standard DDT-a model is shown in Figure 1 in several snapshots illustrating the evolution. We compare the density distribution obtained in the hydrodynamic simulation with the distribution of the tracers. Different colors are used for different ranges of peak temperature of the tracers (i.e., $T_{\rm peak}$, the maximum T reached by a tracer throughout the entire explosion). The tracers marked in black are responsible for the Fe-group production. With their maximum temperature above $T_9 \geqslant 7$ (where T_9 is the temperature in units of 10^9 K) they reach NSE and most of the nucleosynthesis goes to ^{56}Ni or Fe-group nuclei. The gray tracers are instead the main producers of the lighter α-isotopes. In red, green, and blue, we plot the tracers with $T_9 \leqslant 3.7$, the main contributors to the p-process nuclei. Close to the surface of the WD, the peak temperature reached during the explosive phase is not high enough for the nuclei to attain the nuclear statistic equilibrium condition, although significant transmutation of heavy elements into p-process nuclei occurs. The three ranges within this group, $3.0 < T_9 \leqslant 3.7$ (red), $2.4 < T_9 \leqslant 3.0$ (green), and $1.5 \leqslant T_9 \leqslant 2.4$ (blue), are connected to three different behaviors we identify for the production of p-nuclei (see Section 5). This figure shows that there are tracers with low $T_{\rm peak}$ (red) in the inner part of the star, resulting from low-density burning in the deflagration regime. However, the bulk of the *red* tracers is located in the outermost part of the star, together with green and blue tracers, whereas in our models most of the mass has been accreted from a companion and is burned in the delayed detonation models at low densities in the detonation phase.

Recently, Seitenzahl et al. (2010) demonstrated that in two-dimensional SN Ia simulations with 80^2 tracers, all isotopes up to Mo with abundances higher than 10^{-5} are reproduced with an accuracy of 5% (with the exception of ^{20}Ne). We also performed a resolution study, which is discussed in Section 6.5. The nucleosynthesis of the main species obtained with the tracer particle method (i.e., ^{56}Fe, ^{12}C, ^{16}O as well as the mass involved for the p-process nucleosynthesis) is summarized in Table 2. In the last column we report for comparison the abundances for the W7 SN Ia model (Iwamoto et al. 1999).

3.1. *p-process Nucleosynthesis*

The p-process nucleosynthesis is calculated using a nuclear network with 1024 species from neutron and proton up to ^{209}Bi combined with neutron, proton, and α-induced reactions and their inverse. The code used for this work was originally developed and presented by Thielemann et al. (1996). We use the nuclear reaction rates based on the experimental values and the Hauser–Feshbach statistical model NON-SMOKER (Rauscher & Thielemann 2000). Theoretical and experimental electron capture and β-decay rates are from Langanke & Martínez-Pinedo (2000).

The currently favored production mechanism for those isotopes is photodisintegration of intermediate and heavy nuclides. The γ-process becomes effective during the explosive O-burning phase, at $T_9 \geqslant 2.5$, and starts with the photodisintegration of stable seed nuclei. During the photodisintegration period, proton, neutron, and α-emission channels (γ, n), (γ, p), and (γ, α) compete with each other and with β-decays of nuclides far from stability.

In Figure 2, we plot the abundance variations for proton, neutron, and ^{4}He as a function of time for selected tracer particles, at different peak temperatures, in the range between $T_9 = 1.5$ and $T_9 = 3.7$. Comparing with the analogous plot presented in Figure 3 of Kusakabe et al. (2011), we find similar abundances for p, n, and ^{4}He, but the timescales in our explosion model are longer. A difference to note, however, is the double peak for some of the selected tracers. This can be attributed to the fact that our model involves both a deflagration phase and a detonation phase, whereas Kusakabe et al. (2011) employ a pure deflagration model.

In Table 3, we list the 35 p-isotopes with their relative abundance (in %) to the respective elements in the solar system. In Table 4, we list additional isotopes, for which we obtain an important p-contribution—among them the s-only isotopes ^{80}Kr and ^{86}Sr and the neutron magic ^{90}Zr. We also include the neutron-rich isotope ^{96}Zr, which is substantially produced by neutron capture via the ^{22}Ne$(\alpha, n)^{25}$Mg chain during the carbon-burning phase (see Sections 5 and 6.2 for a more detailed discussion). In the same table, we additionally list the neutron magic isotopes ^{86}Kr, ^{87}Rb, ^{88}Sr, and ^{89}Y, which are very abundant in the s-seed and are not affected by photodisintegrations (see Section 6.2). Consequently, these isotopes have to be considered as relics of the s-process seeds.

4. *s*-PROCESS SEEDS

The p-process nucleosynthesis occurs in SNe Ia only if there is an s-process enrichment; therefore, it is essential to determine the s-process enrichment in the exploding WD. In the single-degenerate progenitor model assumed here, there are two sources of s-enrichment: (1) during the AGB phase leading to the formation of the WD, thermal pulses in which s-isotopes are produced occur (TP-AGB phase; see, e.g., Domínguez et al. 2001; Straniero et al. 2006) and (2) thermal pulses during the accretion phase enrich the matter accumulated on the WD (Iben 1981; Iben & Tutukov 1991; Howard & Meyer 1993; Kusakabe et al. 2011). The s-enrichment of the WD in a layer of $\sim 0.1\ M_\odot$ deriving from the past AGB history, prior to the accretion phase, is convectively mixed into the WD (see the discussions of the simmering phase in Piro & Bildsten 2008; Piro & Chang 2008; Chamulak et al. 2008). This dilutes the s-seeds so that their abundances are too low to produce significant yields of p-isotopes. In addition, s-process nucleosynthesis can occur in

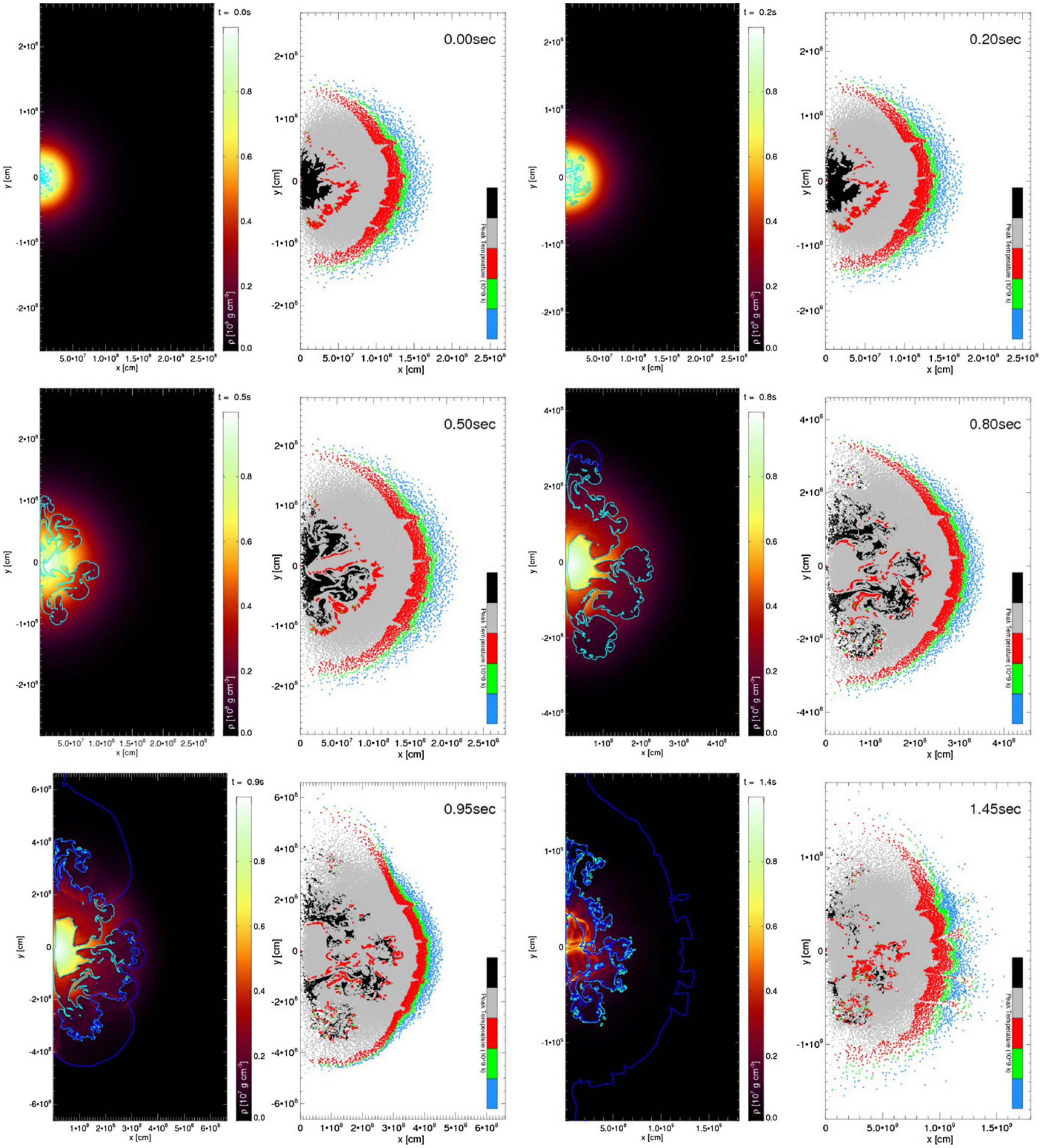

Figure 1. Snapshots from model DDT-a at 0.0 s, 0.2 s, 0.5 s, 0.8 s, 0.95 s, and 1.45 s after ignition. On the left, the hydrodynamic evolution is illustrated by color-coded density and the locations of the deflagration flame (cyan contour) and the detonation front (blue contour). In the model, the first detonation triggers at 0.755 s after ignition. The plots on the right-hand side show the tracer distribution. While the locations correspond to the current time, the color coding is according to the maximum temperature reached during the entire explosion: black tracers peak with $T_9^{\rm peak} > 7.0$; gray tracers with $3.7 < T_9^{\rm peak} < 7.0$; tracers marked in blue ($1.5 < T_9^{\rm peak} < 2.4$), green ($2.4 < T_9^{\rm peak} < 3.0$), and red ($3.0 < T_9^{\rm peak} < 3.7$) are peak temperatures reached in ranges where the *p*-process nucleosynthesis is possible.

the H-rich matter accreted by the CO-WD, due to recurrent He-flashes (Iben 1981), with neutrons mainly produced by the ^{13}C(α, n)^{16}O reaction.

We investigate the influence of different *s*-process abundance distributions for $Z = 0.02$ and $Z = 0.001$ (see Figures 3 and 4) as seeds of *p*-process nucleosynthesis. These distributions are obtained from *s*-process nucleosynthesis calculations with a post-process method (Gallino et al. 1998; Bisterzo et al. 2010). In the AGB scenario, there is a general consensus (Gallino et al. 1998 and references therein) that the main neutron source is the reaction ^{13}C(α, n)^{16}O. In order to activate it, partial mixing of protons from the envelope down into the C-rich layers

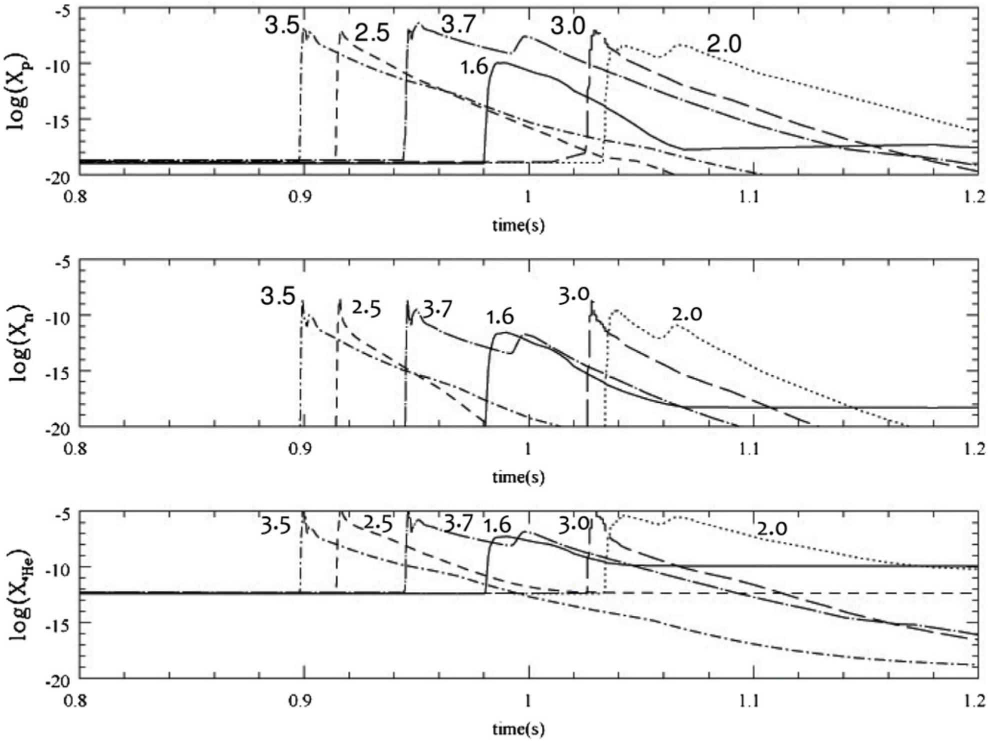

Figure 2. Time evolution of mass fractions of proton (upper panel), neutron (middle panel), and ^{4}He (lower panel), for selected tracers at different peak temperatures (indicated with labels in the panels), i.e., $T_9 = 1.6$, 2.0, 2.5, 3.0, 3.5, and 3.7.

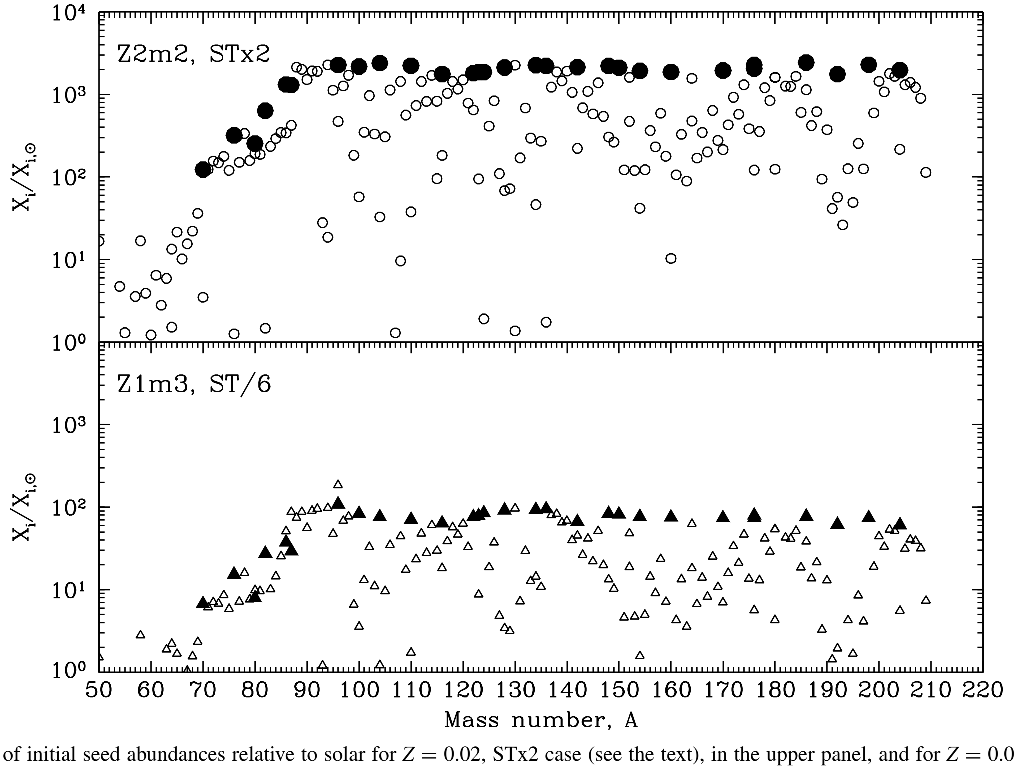

Figure 3. Distribution of initial seed abundances relative to solar for $Z = 0.02$, STx2 case (see the text), in the upper panel, and for $Z = 0.001$, ST/6 case (see the text), in the lower panel. Filled dots and triangles are for *s*-only isotopes.

is required (physical causes of this mixing are discussed by many authors, e.g., Hollowell & Iben 1988; Herwig et al. 1997; Goriely & Mowlawi 2000; Langer et al. 1999; Herwig et al. 2003; Denissenkov & Tout 2003; Cristallo et al. 2009). However, the mass involved and the profile of the ^{13}C-pocket still have to be considered as free parameters, given the difficulty of a realistic treatment of the hydrodynamic behavior at the H/He discontinuity. A series of constraints has been obtained by comparing spectroscopic abundances in *s*-enriched stars at different metallicities with AGB model predictions (see, e.g., Busso et al. 2001; Bisterzo et al. 2010). The spread in the *s*-process yields at each metallicity has been modeled

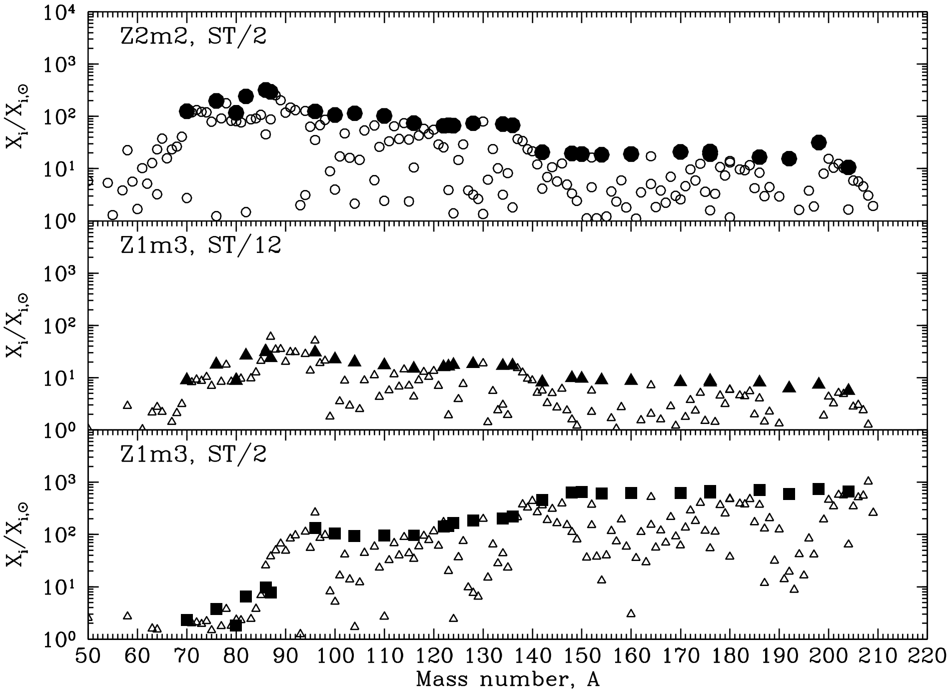

Figure 4. Distribution of initial seed abundances relative to solar for $Z = 0.02$, ST/2 case (see the text), in the upper panel, for $Z = 0.001$, ST/12 case (see the text), in the middle panel, and for $Z = 0.001$, ST/2 case (see the text), in the lower panel. Filled dots, triangles, and squares are for *s*-only isotopes.

parametrically by varying the ^{13}C concentration in the pocket from 0 up to a factor of two times the *standard* value of $\sim 4 \times 10^{-6} M_\odot$ of ^{13}C (Gallino et al. 1998, ST case), and is indicated in Figures 3 and 4 as ST, ST×2 (standard ^{13}C-pocket multiplied by a factor of two), ST/2 (standard ^{13}C-pocket divided by a factor of two), etc. For this work we varied the ^{13}C-pocket concentration in order to obtain a flat *s*-seed distribution, or a non-flat *s*-seed distribution peaked to the lighter or to the heavier *s*-nuclei (see Figures 3 and 4), for both $Z = 0.02$ and $Z = 0.001$.

In Figure 3, we show for two metallicities a typical flat *s*-process distribution (i.e., the isotopes produced mainly by *s*-process nucleosynthesis all have the same overabundance with respect to the solar abundances). The upper panel is a flat *s*-process distribution similar to the one presented by Arlandini et al. (1999, "stellar model") as a best fit to the solar main component. In Arlandini et al. (1999), a full stellar evolutionary model is followed along the TP-AGB phase, using an updated network of neutron captures and beta decay rates (Takahashi & Yokoi 1987; Bao et al. 2000) updated with more recent experimental determinations in the KADONIS database (Dillmann et al. 2006).

The larger number of thermal pulses that in principle can be realized during mass accretion more easily allows the *s*-nuclei to achieve an asymptotic distribution. The difference with respect to the Kusakabe et al. (2011) case B, for a flat distribution in the heavy *s*-only isotope overabundances (about 7000 as compared to our 2000), may be ascribed to different reasons. First, their choice of the neutron capture Maxwellian averaged cross section (MACS) is based on the use of the current 30 keV data. At 30 keV, the MACS of ^{56}Fe, the major seed for the *s*-process, is 11.7 ± 0.4 mb (Bao et al. 2000). However its temperature dependence strongly departs from the usual $1/v$ rule. Actually, the MACS is almost flat between 100 keV and 7 keV (Beer et al. 1992, see their Figure 3). In AGB stellar modes, the major neutron source is the ^{13}C(α,n)^{16}O reaction. Neutrons are released at about 8 keV. Using a value of 30 keV instead is equivalent to doubling the effective MACS of ^{56}Fe. Second, Kusakabe et al. derived the *s*-process distribution using a simplified exponential distribution of neutron exposures. This is in agreement with the classical analysis of the *s*-process, using for the mean neutron exposure parameter the value $\tau_0 = 0.30$ mb^{-1}. The result is a flat distribution for the *s*-only isotopes beyond $A \sim 90$ (Ulrich 1973).

The classical analysis operates at a fixed temperature and neutron density assumed parametrically and using an unbranched s-process flow, not accounting for the much more complex astrophysical situation occurring during recurrent thermal pulses in AGB stars. There, two neutron sources operate at different thermal conditions. The major neutron exposure is activated at $kT \sim 8$ keV by the ^{13}C(α,n)^{16}O reaction in radiative conditions between two subsequent convective thermal instabilities in the top layers of the He intershell (the so-called ^{13}C-pocket). A second neutron exposure results from the marginal activation of the ^{22}Ne(α,n)^{25}Mg reaction in the convective instability at $kT \sim 23$ keV. Moreover, the classical analysis in principle works only for an asymptotic distribution of neutron exposures over a series of identical thermal instabilities and with a constant overlap factor between adjacent pulses. Besides the different thermal and physical conditions, the neutron density is also far from being constant. For an exhaustive comparison see Gallino et al. (1998). Additionally, Kusakabe et al. (2011, their case A) did not consider the neutron poison effect of all light isotopes below ^{32}S, which in particular ignores ^{25}Mg, the most important competitor of ^{56}Fe in neutron capture.

In Figure 4, we present different *s*-process distributions, used as *s*-seeds for this work. In the upper panel, we show an *s*-distribution peaked at the light nuclei (with A between ~75 and ~90). This resembles the pattern obtained from a classical mean neutron exposure with $\tau_0 = 0.15$ mb^{-1}. Similar conditions have been analyzed by Kusakabe et al. (2011). In the middle panel an analogous distribution is shown for $Z = 0.001$.

Table 3
p-Nuclides

Isotope	% Isotopic Abundance	Note	$(X_i/X_{i,\odot})/(^{144}\mathrm{Sm}/^{144}\mathrm{Sm}_\odot)$ [a]
^{74}Se	0.87		0.846
^{78}Kr	0.354		0.716
^{84}Sr	0.56		3.463
^{92}Mo	15.84		0.880
^{94}Mo	9.04		0.149
^{96}Ru	5.51		1.244
^{98}Ru	1.87		1.643
^{102}Pd	0.96		1.092
^{106}Cd	1.215		1.129
^{108}Cd	0.875		0.410
^{113}In	4.28	b	0.032
^{112}Sn	0.96		0.751
^{114}Sn	0.66		0.372
^{115}Sn	0.35	b	0.001
^{120}Te	0.089		0.506
^{124}Xe	0.126		0.997
^{126}Xe	0.115		1.289
^{130}Ba	0.101		1.118
^{132}Ba	0.0097		0.838
^{138}La	0.091		0.041
^{136}Ce	0.193		0.425
^{138}Ce	0.25		0.551
^{144}Sm	3.09		1.000
^{152}Gd	0.20	c	0.017
^{156}Dy	0.0524		0.332
^{158}Dy	0.0902		0.178
^{162}Er	0.136		0.433
^{164}Er	1.56	d	0.116
^{168}Yb	0.135		1.353
^{174}Hf	0.18		1.230
^{180m}Ta	0.0123	e	0.156
^{180}W	0.135		2.633
^{184}Os	0.018		1.156
^{190}Pt	0.0127		0.385
^{196}Hg	0.146		1.581

Notes.

[a] Synthesized mass in the DDT-a model normalized to ^{144}Sm. For the results of this column, see Section 6.2.

[b] ^{113}In and ^{115}Sn, see the text for discussion. Indication for the *r*-process contribution (Dillmann et al. 2008b) is discussed in the text.

[c] ^{152}Gd, *s*-only isotope (Arlandini et al. 1999), due to the radiogenic *s*-branching from ^{151}Sm.

[d] ^{164}Er, *s*-only isotope (Arlandini et al. 1999) due to the branching at ^{163}Dy that is stable at terrestrial conditions, but becomes unstable at stellar temperatures (Takahashi & Yokoi 1987).

[e] ^{180m}Ta, *s*-only isotope (Arlandini et al. 1999) due to the branching at ^{179}Hf. It is stable at terrestrial conditions and becomes unstable at stellar temperatures (Takahashi & Yokoi 1987). The *s*-process feeds ∼50% of the solar ^{180m}Ta. Another substantial contribution to this isotope comes from the νp-process in SNe II (Woosley et al. 1990).

Table 4
s-Nuclides with *p*-Contribution

Isotope	% Isotopic Abundance[a]	Note	$(X_i/X_{i,\odot})/(^{144}\mathrm{Sm}/^{144}\mathrm{Sm}_\odot)$[b]
^{80}Kr	11.7	c	0.803
^{86}Kr	27.0	d	0.142
^{86}Sr	47.0	c	0.786
^{87}Rb	35.3	d	0.181
^{88}Sr	92.3	d	0.418
^{89}Y	92.0	d	0.412
^{90}Zr	72.2	e	0.905
^{96}Zr	55.0	f	2.142

Notes.

[a] Arlandini et al. (1999).

[b] Synthesized mass in the DDT-a model normalized to ^{144}Sm. For the results of this column, see Section 6.2.

[c] ^{80}Kr and ^{86}Sr, *s*-only isotopes. In this work, we find an important contribution from the *p*-process.

[d] ^{86}Kr, ^{87}Rb, ^{88}Sr, and ^{89}Y are relics of the *s*-process seeds.

[e] ^{90}Zr is a neutron magic nucleus at $N = 50$. In this work, we find an important contribution from the *p*-process.

[f] ^{96}Zr in our SN Ia models gets an important contribution by neutron capture during ^{22}Ne-burning.

The lower panel of Figure 4 shows a distribution peaked at heavy isotopes ($A \geqslant 150$), with an important contribution at ^{208}Pb. In Section 6, we discuss in detail the consequences for *p*-process nucleosynthesis using these different distributions of *s*-seeds.

5. DISTRIBUTION OF *p*-NUCLEI

The production mechanism of the various *p*-nuclei can be understood through an analysis of the corresponding nuclear flows. In Figures 5–8, we plot the behavior of the different nuclei versus peak temperature for a solar metallicity case (i.e., DDT-a) using the flat *s*-process distribution shown in Figure 3 (upper panel). In Figure 5, we show ^{12}C, ^{16}O, ^{20}Ne, and ^{22}Ne abundances as a function of T_{peak} for the tracers in the temperature range to produce *p*-nuclei. Starting from the cold outer layers of the star, at $T_9 \simeq 1.4$ ^{22}Ne burns through (α, n) reaction, becoming the most important source of neutrons. This happens at about 0.6 s after ignition of the SN Ia. At $T_9 \simeq 2$, ^{12}C burns mainly via (^{12}C,^{12}C) channels making ^{23}Na, ^{20}Ne, α and *p*-nuclei. At $T_9 \simeq 2.6$, photodisintegration of ^{20}Ne via ^{20}Ne$(\gamma,\alpha)^{16}$O becomes efficient, thus increasing the amount of available ^{16}O. At $T_9 \simeq 3.2$, photodisintegration of ^{16}O becomes efficient. The range of T_9 chosen for Figure 5 is related to the T_9 range where the *p*-process nucleosynthesis occurs.

In Figures 6 and 7, we show the final abundances of all 35 *p*-isotopes listed in Table 3 as a function of peak *T*. In Figure 8, we plot the abundance behavior of the isotopes listed in Table 4, i.e., the *s*-only ^{80}Kr and ^{86}Sr (upper panel), ^{86}Kr, ^{87}Rb, ^{88}Sr, ^{89}Y (middle panel) to be considered as relics of *s*-process seeds with a small contribution from ^{22}Ne burning, and the two special ^{i}Zr isotopes ^{90}Zr and ^{96}Zr (lower panel).

When $T_9 \simeq 2.2$, protons are released by burning of ^{12}C, we find that the first *p*-isotope produced at the lowest T_9 is ^{180m}Ta. A behavior similar to ^{180m}Ta is observed for ^{184}Os, but at somewhat higher temperatures ($2.4 \lesssim T_9 \lesssim 2.5$).

A bit further inside the star, where peak temperatures reach $T_9 \simeq 2.3$–2.4, the *p*-isotopes ^{158}Dy, ^{164}Er, ^{180}W, ^{174}Hf, ^{168}Yb, ^{190}Pt, and ^{196}Hg are produced. This group of isotopes shows a second peak of production at higher *T*, $T_9 \simeq 2.7$. Also ^{152}Gd belongs to this group of *p*-isotopes, but here the second abundance peak at $T_9 \simeq 2.7$ is much lower with respect to the first abundance peak at $T_9 \simeq 2.4$. Note that ^{152}Gd is mainly produced by the *s*-process, as recalled in Section 6.2.

When T_9 exceeds ∼ 3, (γ, p), (γ, α), and (γ, n) become dominant and the lightest *p*-isotopes are produced. ^{74}Se, ^{78}Kr, and ^{84}Sr are synthesized in a wide range of peak temperatures ($3.1 \lesssim T_9 \lesssim 3.6$). Other light *p*-isotopes such as ^{92,94}Mo, ^{96,98}Ru, ^{102}Pd, ^{106}Cd, and ^{112,114}Sn are also produced mostly at $T_9 \geqslant 3$.

In Figure 8, we show the abundance behavior as a function of peak temperature for all isotopes reported in Table 4,

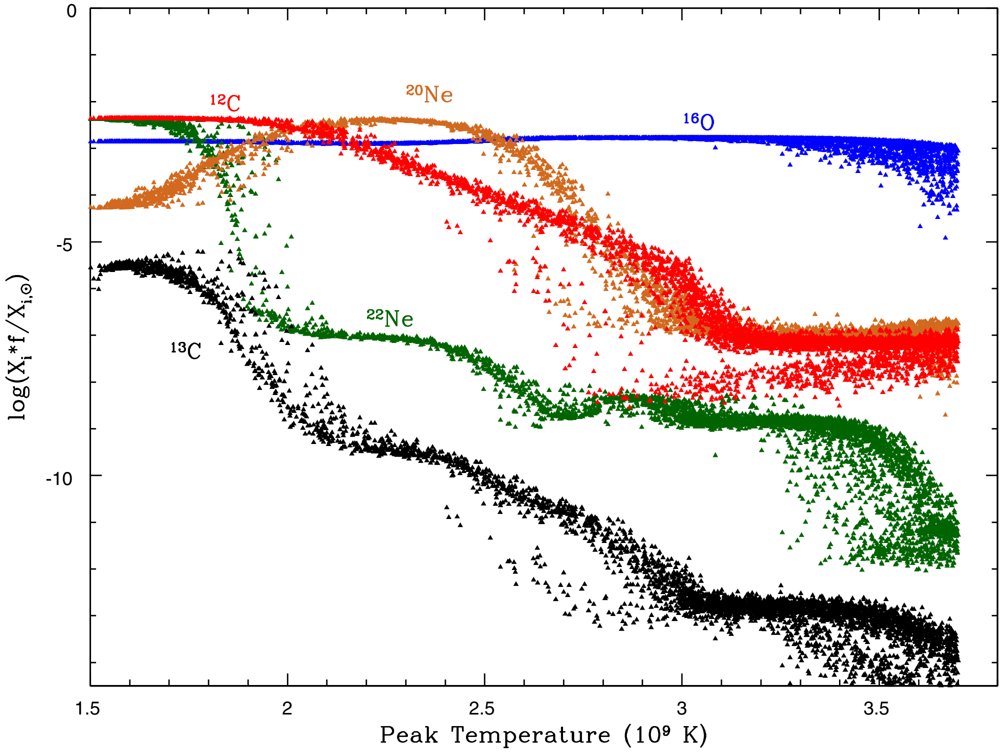

Figure 5. Abundance of ^{12}C (red), ^{16}O (blue), ^{22}Ne (green), and ^{20}Ne (cyan) for tracers selected in the peak T range that allowed p-process nucleosynthesis. This is shown for DDT-a. All the abundances X_i of the three panels are for each tracer, and the f factor in the plot is for $M_{\rm WD}(=1.407\ M_\odot)/N_{\rm tracers}$ (=51,200), i.e., the mass of each tracer.

(A color version of this figure is available in the online journal.)

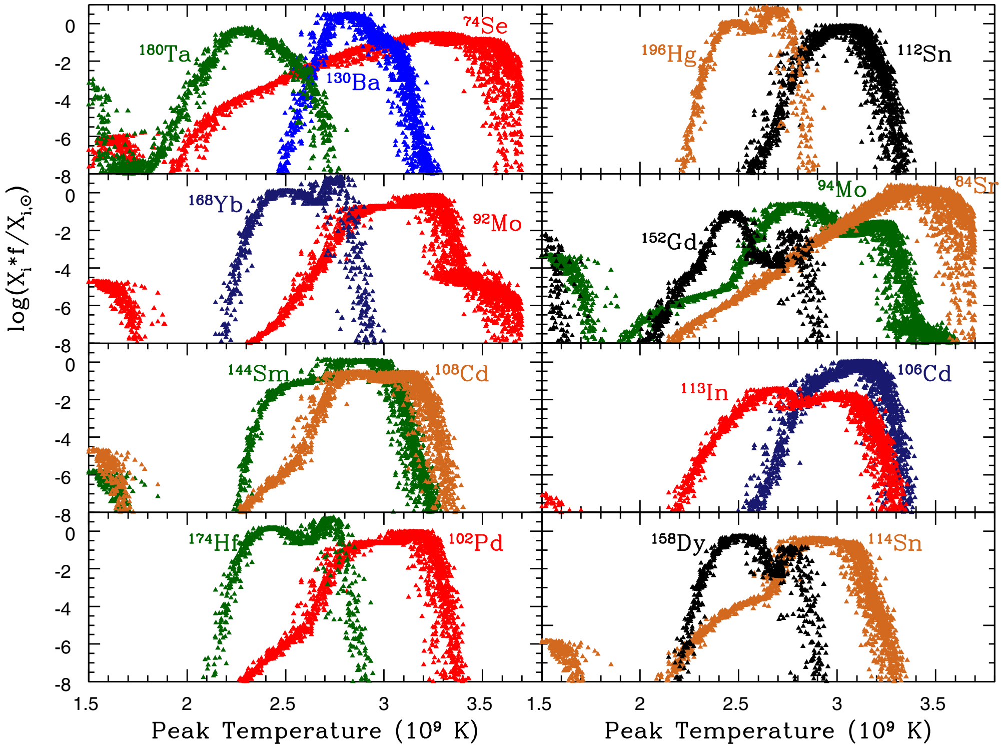

Figure 6. Abundances vs. peak T for tracers selected in the T range that allowed p-process nucleosynthesis. This is shown for DDT-a. The f factor is the same as in Figure 5.

(A color version of this figure is available in the online journal.)

i.e., those where we find (as will be discussed in detail below) an important contribution from p-process nucleosynthesis.

From this figure it is evident that ^{80}Kr and ^{86}Sr (upper panel), and ^{90}Zr (lower panel) are first destroyed by ^{22}Ne burning and

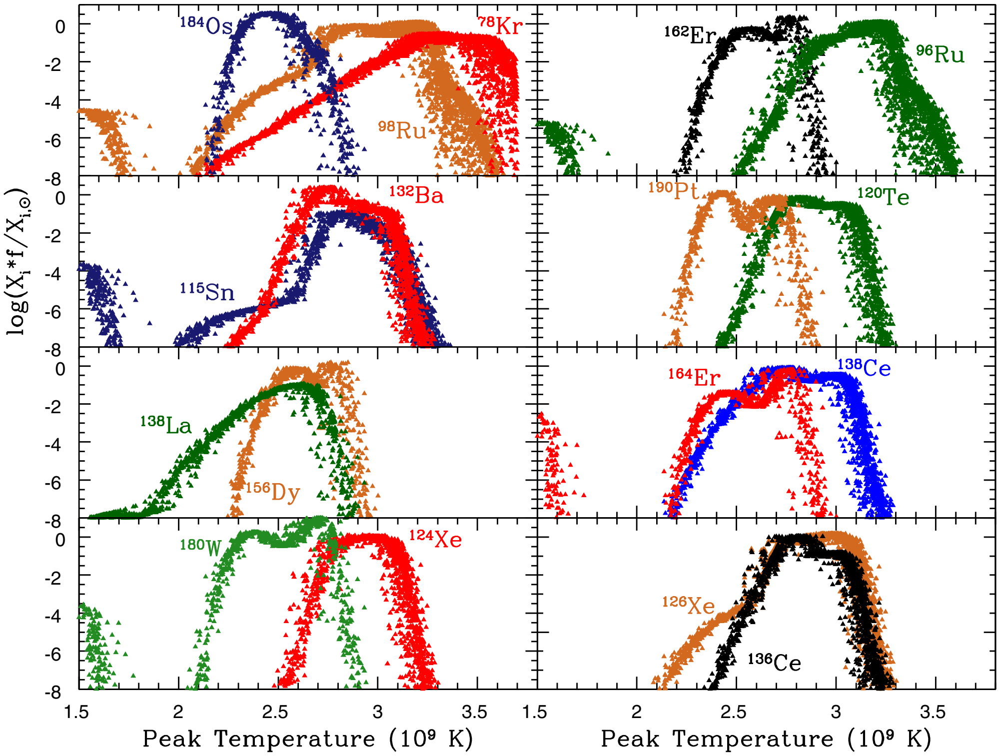

Figure 7. Abundances vs. peak *T* for tracers selected in the *T* range that allowed *p*-process nucleosynthesis. This is shown for DDT-a. The *f* factor is the same as in Figure 5.

(A color version of this figure is available in the online journal.)

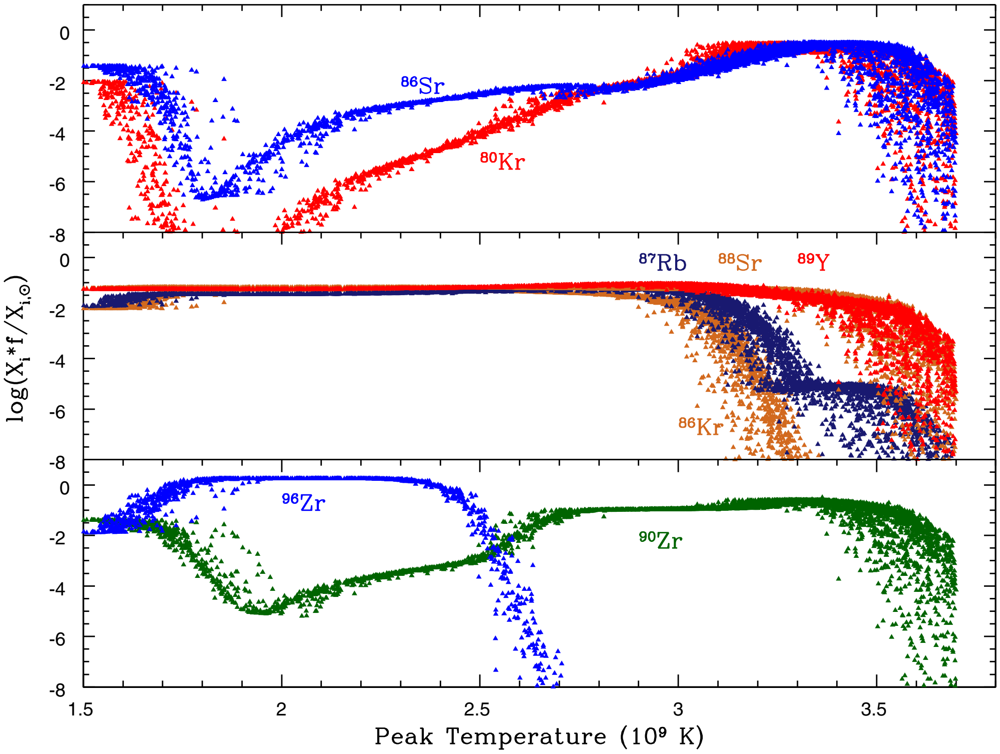

Figure 8. Abundances vs. peak *T* for tracers selected in the *T* range that allowed *p*-process nucleosynthesis. This is shown for DDT-a. The selection of the isotopes in this figure corresponds to the isotopes listed in Table 2. The *f* factor is the same as in Figure 5.

(A color version of this figure is available in the online journal.)

subsequently produced as *p*-nuclei in the ^{12}C-burning phase, at T_9 higher than 2. In contrast, the isotopes in the middle panel, i.e., ^{86}Kr, ^{87}Rb, ^{88}Sr, and ^{89}Y, retain almost their initial values (with small increases in ^{86}Kr and ^{87}Rb) during the ^{22}Ne- and ^{12}C-burning phases, while they are destroyed by photodisintegration at $T_9 \geqslant 3$. Finally, ^{96}Zr (lower panel) is produced at

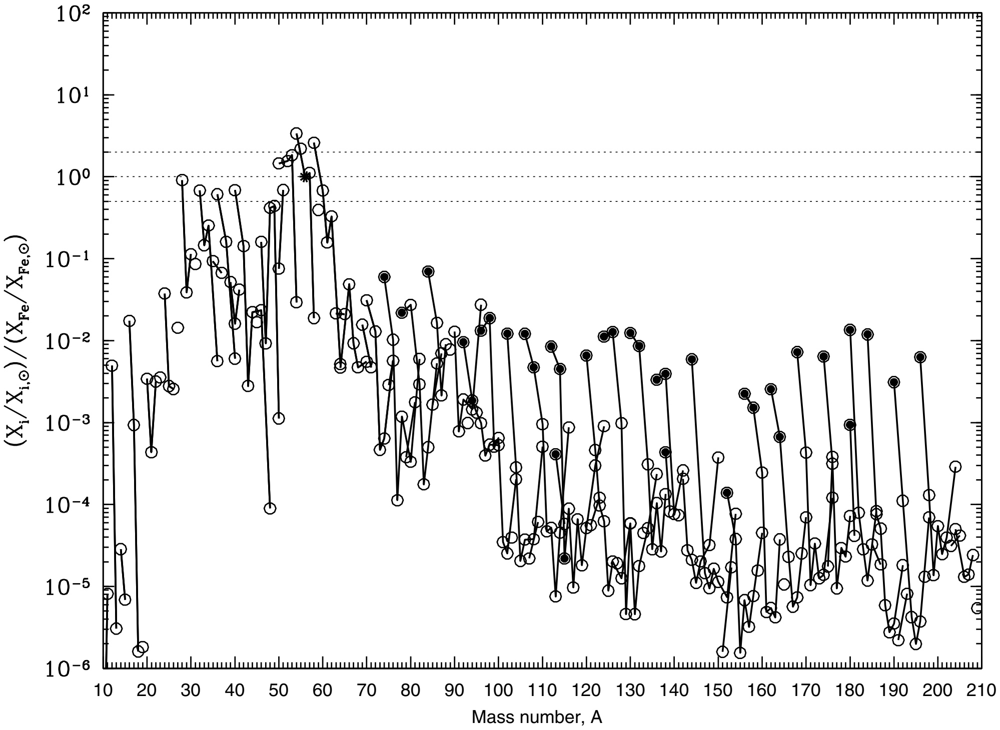

Figure 9. Nucleosynthesis yields (production factors normalized to Fe) obtained using 51,200 tracer particles in the two-dimensional DDT-a model (as described in the text). The ^{56}Fe mass fraction obtained is 0.584 $M_\odot$. The *s*-process enrichment for this test is considered due only to the AGB phase progenitor of the WD. Filled dots are for the *p*-only isotopes (as defined in Table 1). Diamond is for ^{56}Fe.

$T_9 \simeq 1.6$ due to ^{22}Ne burning; in these conditions the neutron density is high and the neutron capture channel on ^{95}Zr is open. Note that the production yield of ^{96}Zr directly depends on the uncertain theoretical Maxwellian neutron capture cross section (MACS) of the unstable ^{95}Zr. In our network we have adopted a factor of two lower than the one reported in the compilation of Bao et al. (2000), taken as the average between the Bao et al. (2000) prescription and the much lower recent theoretical evaluation by the TALYS network of the Brussels database (http//www.astro.ulb.ac.de). Several sources may contribute to the cosmic origin of the most neutron-rich Zr isotope ^{96}Zr (2.8% of solar Zr), i.e., the weak *s*-process in massive stars, the main *s*-process in AGB stars of low and intermediate mass where the ^{22}Ne neutron source is partially activated, and the weak *r*-process during SN II explosion. A further source that can no longer be discarded is now associated with the *p*-process in SN Ia explosions. Clearly, an experimental estimate of the MACS of the unstable ^{95}Zr is of paramount importance.

6. RESULTS AND DISCUSSION

In this section, we present *p*-process nucleosynthesis results obtained with different SN Ia models, exploring different *s*-process distributions and investigating the metallicity effect on the *p*-nuclei production.

6.1. *p-process in WD with AGB Progenitor*

We present the results of the nucleosynthesis calculation for DDT-a, i.e., a delayed-detonation model of a solar metallicity Chandrasekhar-mass WD. We first consider the *s*-process enrichment of the accreting WD as a result of its past AGB history. In this way the mass of ∼0.1 $M_\odot$ enriched in *s*-process elements produced during the AGB phase is spread out over the WD core (following Piro & Bildsten 2008). The resulting nucleosynthesis is presented in Figure 9. Nucleosynthesis calculations with the full network give a ^{56}Fe yield of 0.584 $M_\odot$. This is consistent with what is typically expected for a standard SN Ia (Contardo et al. 2000; Stritzinger et al. 2006). The detonation burns the WD almost completely, and only little ^{12}C and ^{16}O remain in the ejecta. The average *p*-process enrichment we obtain is by a factor of about 50 to 100 below the ^{56}Fe production. From the rough estimate that SNe Ia contribute 2/3 of the total Galactic ^{56}Fe, we conclude that this model cannot account for a significant fraction of the solar *p*-nuclei.

6.2. *p-process in Delayed Detonation Models with s-process in the Accreted Material*

The mass accreted in a close binary system from a hydrogen-rich envelope of a companion onto the CO-WD can be enriched in *s*-process material. As discussed by many authors in the literature, e.g., Sugimoto & Fujimoto (1978), Iben (1981), Nomoto (1982a, 1982b), Iben & Tutukov (1991), and more recently Kusakabe et al. (2011), the accretion rate in the Chandrasekhar-mass progenitor scenario should be sufficiently high to avoid a detonation of He. Recurrent thermal-pulses during accretion, however, are likely to occur (Iben 1981). This *s*-process rich material will act as seed for *p*-process nucleosynthesis during the explosion. In Figure 10, we present our results obtained from the DDT-a model (upper panel) and the DDT-b model (middle and lower panels). Both models, presented in Section 2, involve delayed detonations. The *s*-seeds used are the ones presented in the three panels of Figure 3. The nucleosynthesis yields for $A \geqslant 40$ from model DDT-a (using the *s*-distribution plotted in Figure 3 and marked there as ST×2) are given in Table 5. Since the SN Ia model used is the same as the one presented in the previous section, the resulting nucleosynthesis for nuclei below the Fe group does not differ

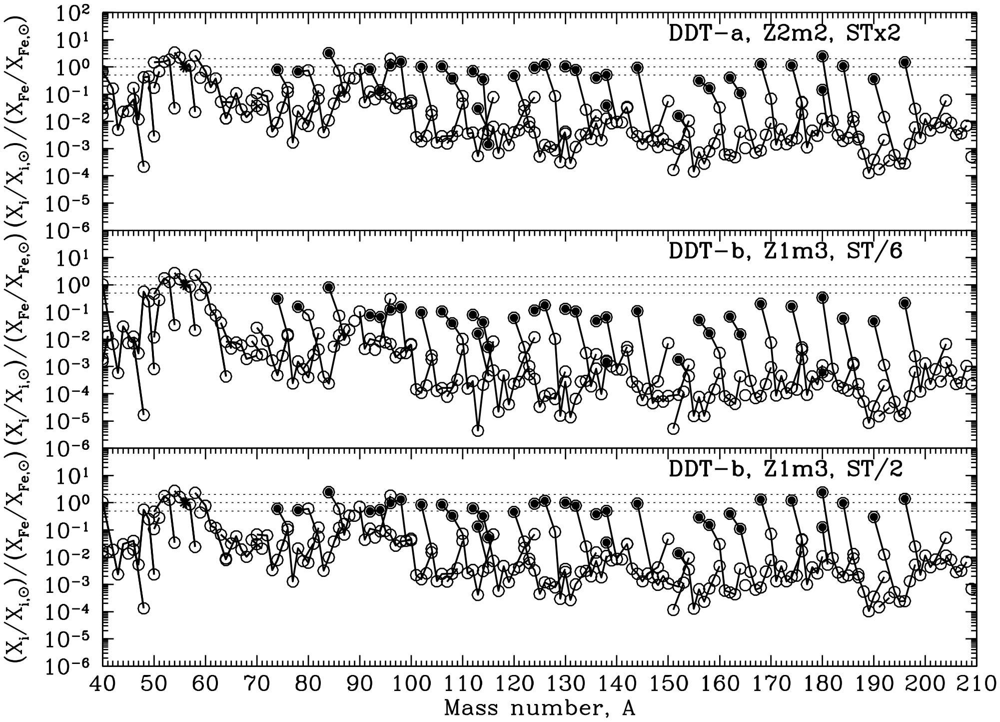

Figure 10. Nucleosynthesis yields (production factors normalized to Fe) obtained using 51,200 tracer particles in the two-dimensional DDT-a model (as described in the text). The *s*-process enrichment for this case has been considered in the accreted mass with solar metallicity (upper panel) and 1/20 solar (middle and lower panels) DDT-b, with the *s*-seed distribution plotted in Figure 3 (upper and lower panels) and in Figure 4 (lower panel). See the text for the explanation of the ^{13}C-pocket strengths adopted.

significantly. The production ratio of the synthesized isotopes normalized to the production ratio of ^{144}Sm (the isotope that has the most similar ratio over solar with respect to ^{56}Fe over solar) is listed in the last column of Table 3 for the "traditional" 35 *p*-nuclei, and in the last column of Table 4 for the other heavy nuclides with an important contribution from the *p*-process in SNe Ia. The problem of the production factors of all isotopes listed in Table 4 will be treated separately, considering the various contributions at the solar system formation through a Galactic Chemical Evolution treatment as in Travaglio et al. (2004).

In Figure 10, we plot the production factor of each isotope *i* normalized to the ratio of ^{56}Fe produced by the model over $(^{56}\mathrm{Fe})_\odot$. We note that for many of the *p*-isotopes the overproduction is at the level of ^{56}Fe. Starting from the lightest *p*-isotopes, ^{74}Se, ^{78}Kr, ^{92,94}Mo, ^{96,98}Ru, ^{102}Pd, and ^{106,108}Cd are produced at the level of ^{56}Fe (within a factor of two). In the case of ^{84}Sr, mainly $^{85}\mathrm{Sr}(\gamma,n)^{84}\mathrm{Sr}$ is active to produce ^{84}Sr at $T_9 \geqslant 2.6$. We test the sensitivity of the production of ^{84}Sr to the uncertainty of the $^{85}\mathrm{Sr}(\gamma,n)^{84}\mathrm{Sr}$ rate. Rauscher & Thielemann (2000) estimate 30% uncertainty of the MACS of this rate at $kT = 100$ keV (the typical temperature for explosive conditions). We find that a small change in the cross section of this reaction changes the final ^{84}Sr abundance by a large factor. This has to be carefully taken into account in *p*-process nucleosynthesis calculations. We also get a high production of ^{86}Sr from *p*-process nucleosynthesis (almost at the level of ^{56}Fe). ^{86}Sr is an *s*-only isotope, contributed by both massive stars (weak component) and by low-mass AGB stars (main component). However, we find a substantial *p*-process contribution to ^{86}Sr.

Despite the historical problem of reproducing the solar abundances of ^{92,94}Mo, ^{96,98}Ru (these isotopes were found neither in comparable abundance with the other *p*-isotopes in SN II nor in SN Ia models or in any other stellar site), we find a good agreement of the abundances of these isotopes with all the other *p*-only isotopes, suggesting SNe Ia as important stellar sites for the synthesis of heavy and light *p*-nuclei. For ^{92}Mo the most important production channel is $^{93}\mathrm{Mo}(\gamma,n)^{92}\mathrm{Mo}$. The second most important chain is $^{96}\mathrm{Ru}(\gamma,\alpha)^{92}\mathrm{Mo}$. A small contribution to ^{92}Mo comes from the (p,γ) channel.

^{94}Mo is mainly synthesized via the (γ,n) photodisintegration chain starting from ^{98}Mo. For $T_9 < 3$ this is almost the only channel to produce ^{94}Mo, while for $T_9 \geqslant 3$ a contribution of ~30% also comes from $^{95}\mathrm{Tc}(\gamma,p)^{94}\mathrm{Mo}$.

Concerning the two Ru *p*-only isotopes, we find that almost 90% of ^{96}Ru is produced in the chain $^{97}\mathrm{Ru}(\gamma,n)^{96}\mathrm{Ru}$, with a small contribution from $^{100}\mathrm{Pd}(\gamma,\alpha)^{96}\mathrm{Ru}$. In contrast, about 50% of the ^{98}Ru is made by $^{99}\mathrm{Ru}(\gamma,n)^{98}\mathrm{Ru}$, and ~50% by $^{99}\mathrm{Rh}(\gamma,p)^{98}\mathrm{Ru}$.

The *p*-contribution to ^{90}Zr mainly derives from $^{91}\mathrm{Nb}(\gamma,p)^{90}\mathrm{Zr}$ and $^{91}\mathrm{Zr}(\gamma,n)^{90}\mathrm{Zr}$.

The other important Zr-isotope in this study, ^{96}Zr, the most sensitive isotope to the neutron density, comes mainly from the neutron capture channel $^{95}\mathrm{Zr}(n,\gamma)^{96}\mathrm{Zr}$, where the necessary neutrons are supplied by the $^{22}\mathrm{Ne}(\alpha,n)^{25}\mathrm{Mg}$ reaction. ^{22}Ne, as shown in Figure 5, burns at very low T_9 ($\simeq 1.7$) in the outermost layers of the star. Therefore, as we will discuss in more detail below, the abundance obtained can be very sensitive to the modeling of the explosion.

Kusakabe et al. (2011) followed the *p*-process nucleosynthesis adopting the W7 C-deflagration model by Nomoto et al. (1984). When we compare these trends with selected trajectories at $T_{9\mathrm{peak}} \simeq 3$ in Figures 1 and 3 of Kusakabe et al. (2011), our results are quite similar in all respects (see below for more details). We also agree with most nucleosynthetic details they discuss. The differences in the total and relative *p*-process yields

Table 5

Synthesized Mass ($M_\odot$) in the SN Ia DDT-a Model (Figure 10, Upper Panel)

Species	Abundance	Species	Abundance	Species	Abundance	Species	Abundance	Species	Abundance	Species	Abundance
^{12}C	1.5671D-02	^{50}Cr	5.4047D-04	^{84}Sr	4.5067D-07	^{115}Sn	1.0004D-09	^{145}Nd	1.8189D-10	^{176}Hf	8.6456D-10
^{13}C	9.2987D-08	^{52}Cr	1.1575D-02	^{86}Sr	1.8400D-06	^{116}Sn	6.0745D-09	^{146}Nd	7.1862D-10	^{177}Hf	7.1442D-11
^{14}N	2.1701D-05	^{53}Cr	1.5783D-03	^{87}Sr	1.4327D-07	^{117}Sn	2.9810D-10	^{148}Nd	4.0872D-10	^{178}Hf	4.3106D-10
^{15}N	2.1673D-08	^{54}Cr	6.6240D-06	^{88}Sr	8.3871D-06	^{118}Sn	6.9873D-09	^{150}Nd	4.9146D-09	^{179}Hf	1.3962D-10
^{16}O	1.4423D-01	^{55}Mn	1.4643D-02	^{89}Y	1.9993D-06	^{119}Sn	6.6589D-10	^{144}Sm	1.3524D-08	^{180}Hf	1.5056D-09
^{17}O	3.0220D-06	^{54}Fe	1.1991D-01	^{90}Zr	5.6021D-06	^{120}Sn	7.5572D-09	^{147}Sm	1.4712D-10	^{180m}Ta	8.1889D-13
^{18}O	2.5498D-08	^{56}Fe	5.8375D-01	^{91}Zr	7.3390D-08	^{122}Sn	6.7889D-09	^{148}Sm	6.1696D-11	^{181}Ta	2.8885D-10
^{19}F	7.1068D-10	^{57}Fe	1.5874D-02	^{92}Zr	2.8426D-07	^{124}Sn	2.6818D-08	^{149}Sm	1.5191D-10	^{180}W	9.6280D-10
^{20}Ne	5.6727D-03	^{58}Fe	4.0790D-05	^{94}Zr	2.3997D-07	^{121}Sb	1.2773D-09	^{150}Sm	4.9988D-11	^{182}W	8.4175D-10
^{21}Ne	1.8643D-06	^{59}Co	6.6528D-04	^{96}Zr	7.7244D-07	^{123}Sb	1.9351D-09	^{152}Sm	1.3103D-10	^{183}W	1.3810D-10
^{22}Ne	3.7666D-04	^{58}Ni	6.4124D-02	^{93}Nb	4.9745D-08	^{120}Te	3.0647D-09	^{154}Sm	1.2263D-09	^{184}W	1.8243D-10
^{23}Na	1.1737D-04	^{60}Ni	6.7264D-03	^{92}Mo	2.5027D-07	^{122}Te	7.4450D-09	^{151}Eu	1.4435D-11	^{186}W	1.3116D-09
^{24}Mg	2.0306D-02	^{61}Ni	7.7360D-05	^{94}Mo	1.6391D-07	^{123}Te	4.2524D-10	^{153}Eu	1.3177D-10	^{185}Re	1.1175D-10
^{25}Mg	1.9054D-04	^{62}Ni	5.2097D-04	^{95}Mo	4.9595D-08	^{124}Te	1.4025D-09	^{152}Gd	1.9977D-11	^{187}Re	2.2337D-10
^{26}Mg	1.9362D-04	^{64}Ni	4.6122D-06	^{96}Mo	3.8125D-08	^{125}Te	2.7803D-10	^{154}Gd	5.7821D-11	^{184}Os	3.0456D-10
^{27}Al	8.2725D-04	^{63}Cu	1.5072D-05	^{97}Mo	9.1247D-09	^{126}Te	1.9648D-09	^{155}Gd	1.3780D-11	^{186}Os	2.5331D-10
^{28}Si	3.3130D-01	^{65}Cu	6.5753D-06	^{98}Mo	3.2686D-08	^{128}Te	2.1474D-09	^{156}Gd	9.6601D-11	^{187}Os	4.1744D-11
^{29}Si	1.1974D-03	^{64}Zn	6.4154D-06	^{100}Mo	1.4678D-08	^{130}Te	1.1202D-08	^{157}Gd	2.8455D-11	^{188}Os	1.3941D-10
^{30}Si	2.5425D-03	^{66}Zn	3.1710D-05	^{96}Ru	1.4367D-07	^{127}I	1.6683D-09	^{158}Gd	1.3021D-10	^{189}Os	3.3415D-11
^{31}P	5.8732D-04	^{67}Zn	1.2094D-06	^{98}Ru	6.5865D-08	^{124}Xe	8.2858D-09	^{160}Gd	7.4789D-10	^{190}Os	1.7001D-10
^{32}S	1.3914D-01	^{68}Zn	2.9505D-06	^{99}Ru	1.3524D-08	^{126}Xe	9.7036D-09	^{159}Tb	1.8889D-10	^{192}Os	1.4298D-09
^{33}S	3.3104D-04	^{70}Zn	2.5358D-07	^{100}Ru	1.6813D-08	^{128}Xe	1.4251D-08	^{156}Dy	1.3456D-10	^{191}Ir	1.0247D-10
^{34}S	3.5648D-03	^{69}Ga	1.1747D-06	^{101}Ru	1.0647D-09	^{129}Xe	6.7265D-10	^{158}Dy	1.2516D-10	^{193}Ir	3.6770D-10
^{36}S	5.6228D-07	^{71}Ga	3.6326D-07	^{102}Ru	1.4012D-09	^{130}Xe	1.1922D-09	^{160}Dy	6.0440D-10	^{190}Pt	1.4588D-10
^{35}Cl	1.5530D-04	^{70}Ge	2.3483D-06	^{104}Ru	7.8273D-09	^{131}Xe	5.0030D-10	^{161}Dy	9.2518D-11	^{192}Pt	3.6798D-10
^{37}Cl	3.2379D-05	^{72}Ge	2.4812D-06	^{103}Rh	1.3001D-09	^{132}Xe	2.3573D-09	^{162}Dy	1.1898D-10	^{194}Pt	6.3110D-10
^{36}Ar	2.3840D-02	^{73}Ge	3.6625D-08	^{102}Pd	1.8434D-08	^{134}Xe	2.7812D-09	^{163}Dy	9.6694D-11	^{195}Pt	3.1544D-10
^{38}Ar	1.4908D-03	^{74}Ge	3.5906D-07	^{104}Pd	4.8247D-09	^{136}Xe	1.0643D-08	^{164}Dy	9.6427D-10	^{196}Pt	2.3987D-10
^{40}Ar	2.2358D-07	^{76}Ge	1.0567D-06	^{105}Pd	6.7008D-10	^{133}Cs	1.9744D-09	^{165}Ho	1.9165D-10	^{198}Pt	1.4554D-09
^{39}K	9.8071D-05	^{75}As	1.9919D-07	^{106}Pd	1.4563D-09	^{130}Ba	8.1235D-09	^{162}Er	2.8935D-10	^{197}Au	6.8591D-10
^{40}K	8.9145D-08	^{74}Se	4.0425D-07	^{108}Pd	1.4541D-09	^{132}Ba	5.8825D-09	^{164}Er	9.0568D-10	^{196}Hg	1.8911D-09
^{41}K	5.9740D-06	^{76}Se	8.9696D-07	^{110}Pd	1.0164D-08	^{134}Ba	4.9567D-09	^{166}Er	5.6222D-10	^{198}Hg	2.4552D-09
^{40}Ca	2.0560D-02	^{77}Se	7.6909D-09	^{107}Ag	5.1444D-10	^{135}Ba	1.1355D-09	^{167}Er	8.5695D-11	^{199}Hg	3.5610D-10
^{42}Ca	3.3420D-05	^{78}Se	3.4351D-07	^{109}Ag	1.4341D-09	^{136}Ba	5.1733D-09	^{168}Er	1.2140D-10	^{200}Hg	2.4156D-09
^{43}Ca	2.1826D-07	^{80}Se	2.1413D-07	^{106}Cd	2.7891D-08	^{137}Ba	1.7809D-09	^{170}Er	7.1327D-10	^{201}Hg	5.2630D-10
^{44}Ca	1.5950D-05	^{82}Se	8.2393D-07	^{108}Cd	7.2676D-09	^{138}Ba	7.1886D-08	^{169}Tm	2.5781D-10	^{202}Hg	2.2432D-09
^{46}Ca	8.8764D-08	^{79}Br	4.8509D-08	^{110}Cd	2.3744D-08	^{138}La	2.7045D-11	^{168}Yb	8.5902D-10	^{204}Hg	3.5097D-09
^{48}Ca	1.5001D-08	^{81}Br	2.1398D-07	^{111}Cd	8.9753D-10	^{139}La	6.6975D-09	^{170}Yb	1.1057D-09	^{203}Tl	8.4790D-10
^{45}Sc	4.6983D-07	^{78}Kr	1.0037D-07	^{112}Cd	2.1349D-09	^{136}Ce	1.4674D-09	^{171}Yb	1.0724D-10	^{205}Tl	2.9824D-09
^{46}Ti	1.9035D-05	^{80}Kr	7.5378D-07	^{113}Cd	1.4926D-10	^{138}Ce	2.5269D-09	^{172}Yb	5.9715D-10	^{204}Pb	1.9311D-09
^{47}Ti	1.2317D-06	^{82}Kr	3.7126D-07	^{114}Cd	2.3586D-09	^{140}Ce	1.6945D-08	^{173}Yb	1.2626D-10	^{206}Pb	4.8271D-09
^{48}Ti	4.4708D-04	^{83}Kr	2.1573D-08	^{116}Cd	1.3732D-08	^{142}Ce	7.8332D-09	^{174}Yb	3.5181D-10	^{207}Pb	6.0427D-09
^{49}Ti	3.6257D-05	^{84}Kr	2.9946D-07	^{113}In	1.6635D-09	^{141}Pr	2.7194D-09	^{176}Yb	1.3185D-09	^{208}Pb	3.3585D-08
^{50}Ti	2.3077D-07	^{86}Kr	1.1256D-06	^{115}In	1.2077D-09	^{142}Nd	1.2709D-08	^{175}Lu	1.8984D-10	^{209}Bi	1.8919D-10
^{50}V	7.8373D-08	^{85}Rb	2.4553D-07	^{112}Sn	3.6123D-08	^{143}Nd	7.0663D-10	^{176}Lu	1.1738D-10		
^{51}V	1.2992D-04	^{87}Rb	3.8945D-07	^{114}Sn	1.1931D-08	^{144}Nd	1.0278D-09	^{174}Hf	6.2584D-10		

may be ascribed to the different numerical accuracy and fine resolution treatment of the explosive nucleosynthesis in the outermost layers, where carbon-burning occurs and where most of the p-nuclei are synthesized. We fully agree with Kusakabe et al. (2011) when they write that *"the yields are very sensitive to the temperature and density trajectories."* The explosive models we follow, especially for the low-temperature trajectories, and the technique we employ for the distribution and the total number of tracers in the outermost regions are probably a major cause of the relative flat distribution among the light, intermediate, and heavy p-process yields, including the reproduction of the most abundant p-nuclei in the Mo and Ru region. Comparison with previous p-calculation presented by Howard et al. (1991) and with more technical details in Howard & Meyer (1993) is somewhat hampered by their parameter study and subdivision in only 15 typical trajectories of the outer region, where they based the post-process calculations on an SN Ia delayed detonation model by Khokhlov (1991).

In order to explain our result, we select two tracers representative of the highest production of ^{92,94}Mo. They have been selected with peak temperature $T_{9\text{peak}} = 3.075$ and 3.180, respectively, corresponding (as one can see in Figure 6) to the maximum production of ^{92}Mo and of ^{94}Mo. The two tracers are located in two different zones of the star, one in the outermost zone, with initial $\rho_{\text{peak}} \simeq 4.0 \times 10^7$ g cm^{-3} (Figure 11, upper panel, dotted line), and the second one a bit further inside the star, with higher initial $\rho_{\text{peak}} \simeq 5.5 \times 10^8$ g cm^{-3} (Figure 11, upper panel, solid line). The inner tracer is first reached by the deflagration wave, and has an initially rather high density. When it is finally reached by the detonation, it has much lower density

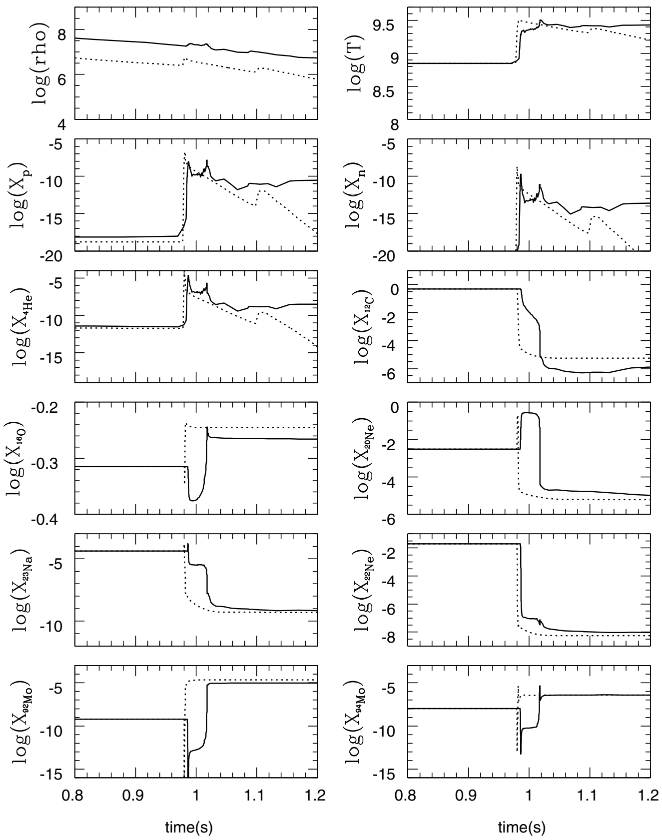

Figure 11. Time evolution of density and temperature (upper panels), of mass fractions of proton and neutron (second panels from the top), ^{4}He and ^{12}C (third panels from the top), ^{16}O and ^{20}Ne (fourth panels from the top), ^{23}Na and ^{22}Ne (second panels from the bottom), and ^{92}Mo and ^{94}Mo (lower panels). The solid and dotted lines are for two different tracers.

due to the pre-expansion. The time on the plot starts at 0.8 s (the time at 0 s corresponds to the start of the deflagration wave). In the other panels of this plot are shown the mass fractions of p, n, ^{4}He, ^{12}C, ^{16}O, ^{20}Ne, ^{23}Na, and ^{22}Ne, and in the lower panels the mass fractions of ^{92}Mo and ^{94}Mo. Looking at ^{92}Mo and ^{94}Mo (lower panels), one can see that, despite the two different histories of the tracers, these isotopes are produced with very similar abundances in these two tracers. In fact, the initial density and temperature are quite different at $t \simeq 0.0$ s, but, due to the expansion of the star, they are quite similar at the time of the production of ^{92}Mo and of ^{94}Mo. The initial ^{12}C set with the same value for all tracers falls abruptly when the detonation wave passes through. Consequently, ^{23}Na is produced, and ^{20}Ne at the beginning of C-burning is mostly dissociated, producing α and ^{12}C. As to ^{22}Ne, at the time of ^{92}Mo and ^{94}Mo formation, it is strongly reduced with respect to the initial value, with a consequently low production of neutrons in the region where the light-p are produced. After a detailed analysis of the nucleosynthesis that deals with the production of the p-nuclei, we can state that an accurate treatment of the outermost region of the SN Ia model is at the base of these results.

Going further to higher mass number, we note an underproduction in the Cd–In–Sn region. The origin of the rare odd isotopes ^{113}In and ^{115}Sn (and, related to these, ^{112}Sn and ^{114}Sn) is debated. These rare nuclei are shielded from the two dominant nucleosynthesis processes for heavy elements: the s-process flow proceeds via $^{112}\mathrm{Cd} \longrightarrow {}^{113}\mathrm{Cd} \longrightarrow {}^{114}\mathrm{Cd} \longrightarrow {}^{115}\mathrm{In} \longrightarrow {}^{116}\mathrm{Sn}$, thus bypassing the rare nuclei, except for small branchings of the reaction path at ^{113}Cd, ^{115}Cd, and ^{115}In, which may contribute to the abundances of ^{113}In, ^{114}Sn, and ^{115}Sn. The β-decay chains from the r-process region are shielded by the neutron-rich Cd and In, but may also feed the rare nuclei via minor decay branchings at ^{113}Cd and ^{115}Cd (Rayet et al. 1990; Howard et al. 1991; Theis et al. 1998). In a previous investigation of the s- and r-process components of the Cd-, In-, and Sn-isotopes, Nemeth et al. (1994) suggested that the rare isotopes in the $A = 112$–115 region may be produced by a complex interplay of s- and r-processes. According to Dillmann et al. (2008b), the s-process contribution to ^{113}In and ^{115}Sn is excluded as well as the thermally enhanced β-decay by an accelerated decay of the quasi-stable ^{113}Cd and ^{115}In during the s-process (the mechanism proposed by Nemeth et al. 1994). The most promising scenario suggested by Dillmann et al. (2008b) is related to β-delayed r-process decay chains. Nevertheless, uncertainties in nuclear physics have to be taken into account.

Moving to the intermediate p-isotopes, we note ^{138}La and ^{180m}Ta are far below the average p-nuclei production (by a factor of ~50 and ~8, respectively). The astrophysical origin of the two heaviest odd-odd nuclei ^{138}La and ^{180m}Ta has been discussed over the last 30 years (Woosley & Howard 1978; Beer & Ward 1981; Yokoi & Takahashi 1983; Woosley et al. 1990; Rauscher et al. 2002), more recently by Cheoun et al. (2010). We derive a rather small contribution from SNe Ia. ^{180m}Ta receives an important contribution from the s-process due to the branching at ^{179}Hf, a stable isotope that becomes unstable at stellar temperatures (Takahashi & Yokoi 1987). There is also a second branching at ^{180m}Ta due to the fact that ^{179}Hf has a small n-capture branching to ^{180m}Hf, which at $T_9 \simeq 0.3$ is not thermalized and quickly decays to ^{180m}Ta (Beer & Ward 1981; see also Mohr et al. 2007; Käppeler et al. 2004). In a core-collapse supernova, ^{180m}Ta is synthesized by the neutrino process (Woosley et al. 1990). Independent of the production mechanism, according to Mohr et al. (2007), freeze-out from thermal equilibrium occurs at $kT \simeq 40$ keV, and only ~35% of the synthesized ^{180m}Ta survives in the isomeric state. Consequently, in all supernova results, the yield obtained so far without accounting of the freeze-out effect of excited levels discussed by Mohr et al. (2007) and Hayakawa et al. (2010b) should be decreased by about 2/3. Hayakawa et al. (2010b) positively cited the Mohr et al. (2007) evaluation, writing that *the isomeric residual population Ratio R* by Mohr et al., i.e., $R = P_m/(P_g + P_m) = 0.35 \pm 0.04$. It was based *"from an estimate of the freeze-out temperature without following the time-dependent evolution in detail."* The new result by Hayakawa et al. (2010b), i.e., $R = 0.38$, essentially coincides with $R = 0.39 \pm 0.01$ given by Hayakawa et al. (2010a). The new problem resides in the conclusion given by Hayakawa et al. (2010b), *"the main conclusion of the previous study by Hayakawa et al. (2010a) is thus strengthened: the solar abundances of ^{138}La and ^{180m}Ta relative to ^{16}O can be systematically reproduced by neutrino nucleosynthesis and an electron neutrino temperature of kT close to 4 MeV."* Taken at face value, this sentence contrasts first with the fact that the s-process already produces about 50% of solar ^{180m}Ta (Mohr et al. 2007), whereas no s-process ^{138}La is predicted, and second with our present p-process SN Ia result that further provides extra p-contribution to solar ^{180m}Ta (and to ^{138}La). Note that in Figure 10 there are two p-process nuclides at $A = 180$; the higher one is ^{180}W (which in turn is only produced by the s-process at the level of 5% (see the review by Käppeler et al. 2011). The conclusion by Hayakawa et al. (2010b) should, however,

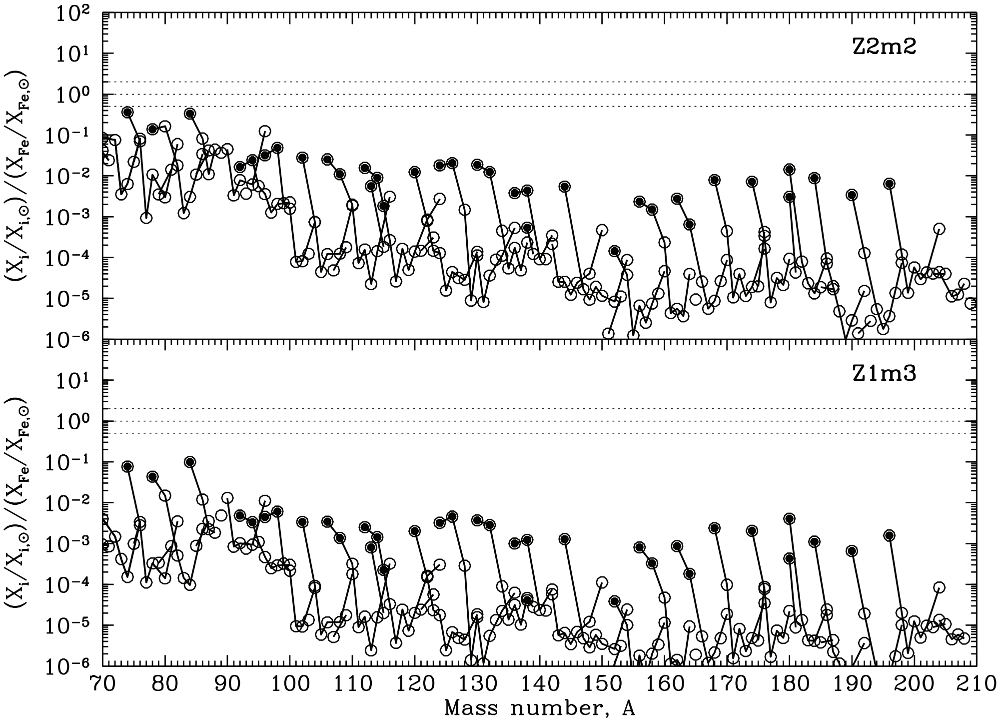

Figure 12. Nucleosynthetic yields (production factors normalized to Fe) obtained using 51,200 tracer particles in the two-dimensional DDT-a model (as described in the text). The *s*-process enrichment in the accreted mass for this case has been considered with solar metallicity (upper panel) and 1/20 solar (lower panel) DDT-b, with the non-flat *s*-seed distribution plotted in Figure 4 (upper and middle panels, respectively).

account for the uncertainties in the stellar neutrino cross sections involved in the production of ^{180m}Ta and ^{138}La.

Concerning ^{152}Gd and ^{164}Er, we have already outlined that both isotopes are mainly reproduced by the *s*-process (Arlandini et al. 1999), through the branching at ^{151}Sm (see updates in Marrone et al. 2006) and through the branching at ^{163}Dy, another stable isotope that becomes unstable at stellar temperatures (Takahashi & Yokoi 1987). No production of ^{152}Gd is expected by the weak *s*-process in massive stars since it is strongly destroyed during carbon-shell burning (see The et al. 2007 and references therein). We find that ^{152}Gd is produced by a factor of 100 less than the average *p*-distribution, which confirms the non-*p* astrophysical origin of this isotope. Also ^{164}Er is underproduced by one order of magnitude with respect to the heavy *p*-nuclei. Both ^{152}Gd and ^{164}Er are to be classified as *s*-only isotopes, not *p*-only.

6.3. *Different s-process Distributions*

Using the *s*-process seeds plotted in Figure 4 (upper and middle panels), corresponding to a non-flat *s*-distribution, peaked to the lighter *s*-isotopes with $A \sim 80$–90), the nucleosynthesis results are shown in the two panels of Figure 12. Concerning the *p*-nuclei, we note that with an *s*-seed distribution that is flat (see Figure 3, upper and lower panels) or peaked to the lighter *s*-isotopes (see Figure 4, upper and middle panels), almost all *p*-nuclei scale linearly with metallicity (within a factor of ∼2), with the exception of the three lightest *p* nuclei ^{74}Se, ^{78}Kr and ^{84}Sr, and ^{180m}Ta, which show a different behavior. While a decrease of ^{74}Se, ^{78}Kr, and ^{84}Sr by a factor of ∼20 would be expected when changing the metallicity from solar to $Z = 0.001$, we observe a variation by a factor of only ∼2. For ^{180m}Ta, by decreasing metallicity by a factor of 20 (from solar down to $Z = 0.001$) we obtain an increase of the *p*-process contribution of a factor of ∼10, still far below the average *p*-nuclei abundance obtained for these models.

Particular attention has to be devoted to the *s*-distribution plotted in Figure 4 (lower panel) peaked to the heavier *s*-isotopes. In this case, the *p*-nuclei on average are produced at the level of ^{56}Fe, when normalized to solar abundances (see Figure 10, lower panel).

6.4. *^{208}Pb as Seed of p-nuclei*

In order to check in greater detail the effect of the *s*-process seed on the resulting *p*-nuclei, we run a further test for model DDT-a. We adopt solar *s*-process abundances except for ^{208}Pb, for which we use the value from the ST×2 distribution (shown in Figure 3, upper panel). If a significant fraction of the seed abundances is present in the form of Bi- and Pb-isotopes, they are converted to nuclei of lower mass by photodisintegration sequences starting with (γ, n) reactions (Dillmann et al. 2008b). As could be expected, we obtain an important *p*-contribution (of ≃60%) to ^{144}Sm and ^{196}Hg using the ^{208}Pb *s*-enhanced seed. Also ^{168}Yb, ^{174}Hf, and ^{190}Pt get a substantial contribution (about 25%–30%) this way. No important contribution derives on the light *p*-nuclei in this case.

6.5. *Resolution Study*

We perform a resolution study for model DDT-a, testing whether the number of tracer particles used for our calculation is sufficient to obtain converged nucleosynthesis predictions. Since we are interested in the convergence of the *p*-process yields, this could be achieved in an efficient way (for general convergence tests, see Seitenzahl et al. 2010). Instead of increasing the number of tracer particles, we reduce the mass represented by each tracer in the *p*-process region with the variable tracer mass method (Seitenzahl et al. 2010). The resolution

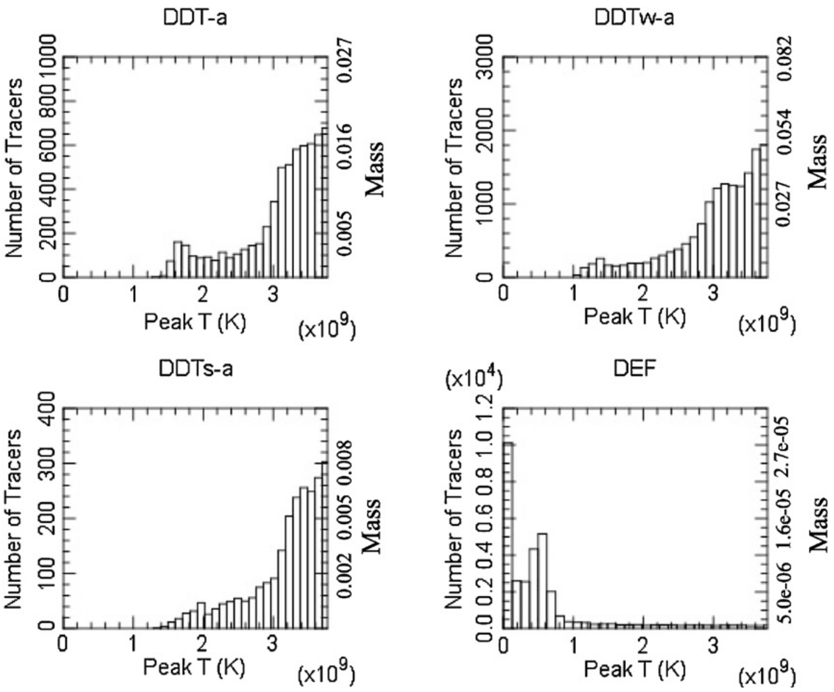

Figure 13. Mass distribution (plotted in the form of number of tracers) as a function of peak temperature. The upper left panel is for the DDT standard model, the upper right panel is for the weaker DDT model, the lower left panel is for the stronger DDT model, and the lower right panel is for the deflagration model. On the right side of each box is reported the mass distribution (in $M_\odot$) as a function of peak temperature.

study consists of a run of the same DDT-a model, but computed with variable tracer masses. The p-process mass covered in the DDT-a standard model is $\sim 0.13\,M_\odot$ with tracer particles with a constant mass of $2.75 \times 10^{-5}\,M_\odot$. In the resolution test performed we cover $\sim 0.2\,M_\odot$ in the p-process temperature range, and the tracer particles have masses in the range $1.13 \times 10^{-5}\,M_\odot$ and $4.90 \times 10^{-5}\,M_\odot$. Between the two cases the resulting p-process abundances differ by only a few percent. Therefore, we can consider our DDT-a model (and all the other models presented in this paper) well resolved for the p-process calculations.

6.6. *Pure Deflagration and Different Strengths of Delayed Detonations: Consequences for the p-process*

In addition to our "standard case" DDT-a, we perform p-process nucleosynthesis calculations for the other SN Ia models presented in Section 2, i.e., pure deflagration and delayed detonations of different strengths. In Figure 13, we show the mass distribution (in the form of tracer particles) at different $T_{\rm peak}$ (in the temperature range of p-process nucleosynthesis). In the pure deflagration case (DEF-a) it is clear from the histogram that much mass remains unburned (below $T_9 \simeq 1$) (as was also discussed in greater detail in Travaglio et al. 2004, where only deflagration models were presented). Consequently, in this case we have a factor of $\sim$10 more ^{22}Ne, which results in a much higher neutron abundance and, thus, the nuclei most sensitive to the neutron density (e.g., ^{54}Fe, ^{58}Ni, ^{96}Zr) show major overproduction. It is also important to note that in the DEF-a model, ^{92}Mo, ^{96}Ru are lower than the DDT-a model (using the same initial s-process distribution) by a factor of $\sim$3, and ^{74}Se, ^{78}Kr, and ^{84}Sr by a factor of $\sim$2. This effect can be attributed to the different distributions of mass in the two models. In fact, the amount of mass (corresponding to the number of tracers) at $T_9 \geqslant 3$ in the DDT-a model is a factor of $\simeq$3 higher than that in the DEF-a model. For ^{168}Yb, ^{174}Hf, ^{180}W, ^{184}Os, and ^{196}Hg, we observe the opposite effect. We see that in the DEF-a model these heavy p-isotopes are more abundant by a factor between two and three with respect to the DDT-a case. From Figure 13 we note that the mass in the range $T_9 \sim 2.5$–2.7 (as shown in Figures 6 and 7, this is the T zone with the highest production of these isotopes) is a factor of $\sim$2 lower for the DDT model with respect to the DEF-a model. From this we conclude that the mass distributions and therefore the underlying SN Ia model can introduce rather important changes in the final p-process nucleosynthesis.

For the pure-deflagration SN Ia model (DEF-a), the results of the nucleosynthesis calculations are shown in Figure 14 (lower panel) for all isotopes with $A \geqslant 40$. The s-process initial seeds used are the ones plotted in Figure 3 (upper panel). Figure 14 also gives the results for two other DDT models. As was pointed out by Röpke & Niemeyer (2007), Mazzali et al. (2007), and Kasen et al. (2009), it is possible to cover a wide range of ^{56}Ni masses with this class of models. The variation is introduced by different ignition geometries that set the strength of the initial deflagration phase and thus pre-expand the WD prior to detonation triggering to variable degrees. Apart from the DDT-a model discussed in previous sections, we calculate the nucleosynthesis for two additional delayed detonation models, one with a stronger (DDTs-a) and one with a weaker (DDTw-a) detonation phase (details of these models are given in Section 2). For the DDTw-a (Figure 14, upper panel), we note a much higher production of the light and intermediate p-nuclei (up to a factor of $\sim$5 for ^{84}Sr). This is mainly connected to the distribution of tracers, for $T_9 \geqslant 3$. In fact, as shown in Figure 13, with respect to DDT-a the DDTw-a model has two to four times more tracer particles in the high-T p-region, where most of the light p-nuclei are produced. A smaller effect is seen for the heavier p-nuclei. They are produced at lower T_9 ($\simeq$2), where the difference between the two tracer distributions is not as high as in the highest T_9 zones. Nevertheless, using for DDT-a

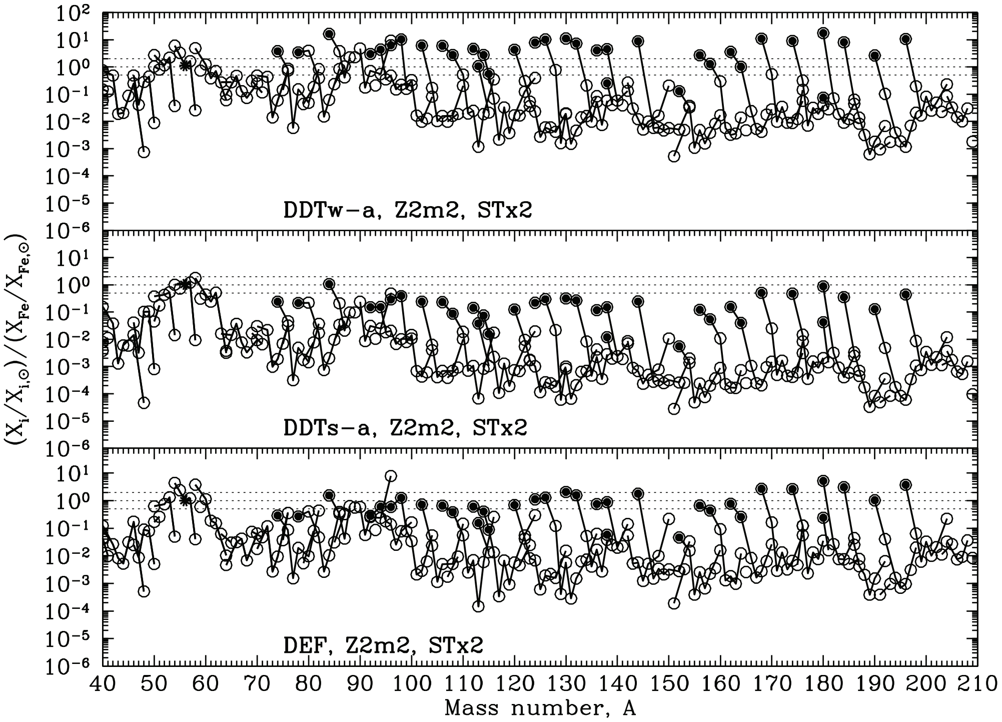

Figure 14. Nucleosynthesis yields (production factors normalized to Fe) obtained using 51,200 tracer particles in the 2D weaker (upper panel, DDT-w) and stronger (middle panel, DDT-s) delayed detonation models, and the pure deflagration model (lower panel, DEF-a) (as described in the text). The *s*-process enrichment for this case is considered in the accreted mass, with the distribution plotted in Figure 6, upper panel.

and DDTw-a the same *s*-process seed abundances, we obtain an almost flat distribution for the resulting *p*-nuclei, including the lightest ones. It is important to note that in the case of DDTw-a we significantly increase ^{113}In and ^{115}Sn, producing them at the same level as ^{56}Fe (within a factor of ∼2).

For the DDTs-a model, we find generally lower abundances of the *p*-nuclei. This is due to the fact that much less mass is in the low-*T* region where the *p*-process can occur, and most of the material reaches NSE condition, mainly producing ^{56}Fe (as indicated in Table 2). Nevertheless, on average the *p*-nuclei show an almost flat distribution (deriving from the same distribution of the *s*-process seeds).

7. CONCLUSIONS AND FUTURE WORK

We have presented results of detailed nucleosynthesis calculations for two-dimensional delayed detonation and deflagration SN Ia models, focusing in particular on *p*-process nucleosynthesis. We used initial abundances of *s*-nuclei synthesized during the past AGB history of the WD and during the mass accretion phase. During the late AGB phase of the companion, about 0.1 $M_\odot$ of the CO-core become enriched in *s*-process elements by the effect of recurrent He-shell thermal instabilities. About 1000 years before the explosion, the simmering phase induced by central C-burning dilutes the *s*-rich material by a factor of ∼10 over the whole WD. The corresponding *p*-process yield is negligible when integrated over the whole ejecta. In contrast, the *s*-seeds synthesized during the WD mass accretion phase may give rise to an average *p*-process overabundance in the ejecta comparable with that of ^{56}Fe. Neutron fluxes available for the *s*-process in the accreted material rely on the activation of the $^{13}C(\alpha,n)^{16}O$ reaction during the convective He flashes. This applies under the assumption that a small amount of protons are ingested in the top layers of the He intershell, as was suggested by Iben (1981). Protons are captured by the abundant ^{12}C and converted into ^{13}C via $^{12}C(p,\gamma)^{13}N(\beta^{+}\nu)^{13}C$ at $T \sim 1 \times 10^{8}$ K. Neutrons are then released in the bottom region of the convective He intershell by $^{13}C(\alpha,n)^{16}O$. In contrast to the previous AGB phase, where both the formation of the ^{13}C-pocket and the subsequent release of neutrons occur radiatively in the interpulse phase, here the *s*-process is made directly in the convective shell during thermal instability, similar to the *plume mixing* by Ulrich (1973). The results of our post-process calculations should be considered as preliminary, given the general difficulty of following with full evolutionary codes the peculiar conditions of thermal pulses during the mass accretion phase.

In the cases of *s*-seeds from the mass accretion phase, we analyzed different SN Ia models, i.e., delayed detonations of different strengths, and a pure-deflagration model. For all these models we explored different *s*-process distributions and their consequences for the *p*-process. We also investigated a metallicity effect of the *p*-process nucleosynthesis in this scenario, considering models with solar metallicity and 1/20 solar. Despite the fact that studies of *s*-process nucleosynthesis during the accreting WD phase are led by the need to clarify the effective *s*-process distribution in these particular conditions, the results presented in this paper for *p*-process nucleosynthesis are quite significant. Note that a flat *s*-seed distribution directly translates into a flat *p*-process distribution whose average production factor scales linearly with the adopted level of the *s*-seeds. In contrast to previous work on *p*-process nucleosynthesis in SNe Ia (e.g., Kusakabe et al. 2005, 2011; Goriely et al. 2002, 2005), we demonstrated that we can produce almost all the *p*-nuclei with similar enhancement factors relative to ^{56}Fe, including the puzzling light *p*-nuclei ^{92,94}Mo, ^{96,98}Ru. We found that only the isotopes ^{113}In, ^{115}Sn, ^{138}La, ^{152}Gd, and ^{180m}Ta diverge from the average *p*-process production. Among them, ^{152}Gd and ^{180m}Ta have an important contribution from the *s*-process in AGB stars (Arlandini et al. 1999) or the neutrino process in SNe II (Woosley et al. 1990; Wanajo et al. 2011a). Both ^{113}In and ^{115}Sn are not fed by the p-process nor by the s-process. For these, we refer to the discussion by Dillmann et al. (2008a).

As far as the Galactic chemical evolution of p-nuclei is concerned, our results lead to the following very preliminar conclusions. Given the assumption of different s-seed distributions (see Figures 3 and 4), for both solar metallicity and 1/20 solar, we could show that the p-nuclei on average are produced at the level of ^{56}Fe when normalized to solar abundances (as shown in Figure 10). Even taking a fixed choice of the ^{13}C-pocket at different metallicities, since the s-seed distributions peaked at heavier mass numbers are on average dominant, we may infer that the $(p/^{56}\mathrm{Fe})/(p/^{56}\mathrm{Fe})_\odot$ ratio is always constant. This suggests the primary nature of the p-process. This aspect will be examined thoroughly in a forthcoming paper. From the hypothesis that SNe Ia are responsible for 2/3 of the solar ^{56}Fe, and by assuming that our DDT-a model represents the typical SN Ia with a frequency of ~70% of all SNe Ia (Li et al. 2011), we conclude that they may be responsible for about 50% of the solar abundances of all p-nuclei. Instead, if we consider an average between DDTw-a and DDTs-a models, considering that they represent ~10% of all SNe Ia (Li et al. 2011), still with a flat s-seed distribution (see Figure 14), we obtain that they may account for 75% of the solar abundances of all p-nuclei. Of course, these are the first rough estimates of how SNe Ia, in principle, can contribute to the solar system composition of p-nuclei. These results must also take into account that SNe II can be potentially important contributors to the galactic p-nuclei. Rayet et al. (1995) showed that about 1/4 of the solar system p-nuclei can be attributed to SN II explosions. Later, Woosley & Heger (2007) showed that p-nuclei can have an appreciable contribution at the solar composition from explosive neon and oxygen burning for a mass number greater than 130, but are underproduced for lighter masses. As recalled in Section 1, recent works on the νp-process in SNe II show that a non-negligible contribution may come from this process to the light p-isotopes.

A more thorough analysis of the role of SNe Ia in the solar composition of p-nuclei is planned.

Finally, we note that recent works (e.g., Sim et al. 2010; Fink et al. 2010; and references therein) discussed the fact that the explosion of sub-Chandrasekhar mass WDs via the double detonation scenario is a potential explanation for SNe Ia (but see Woosley & Kasen 2011). Again, the possibility of p-process production will be explored in a forthcoming paper.

All the tables with the yields obtained for different models presented in this work are available upon request.

We thank S. Cristallo and O. Straniero for many discussions of the feasibility of the s-process during mass accretion. We thank U. Battino for testing the production channels of the various p-isotopes on the occasion of his Master's degree. We thank P. Mohr for an extremely detailed update of the nucleosynthesis of ^{180m}Ta and ^{138}La in explosive SN conditions. Thanks are due to the anonymous referee for the comments that helped improve the paper. This work has been supported by B2FH Association. The numerical calculations have also been supported by Regione Lombardia and CILEA Consortium through a LISA Initiative (Laboratory for Interdisciplinary Advanced Simulation) 2010 grant. This work was partially supported by the Deutsche Forschungsgemeinschaft via the Transregional Collaborative Research Center "The Dark Universe" (TRR 33), the Emmy Noether Program (RO 3676/1-1), and the Excellence Cluster "Origin and Structure of the Universe" (EXC 153).

REFERENCES

Arcones, A., & Janka, H.-T. 2011, A&A, 526, 160

Arcones, A., & Montes, F. 2011, ApJ, 731, 5

Arlandini, C., Käppeler, F., Wisshak, K., Gallino, R., Lugaro, M., Busso, M., & Straniero, O. 1999, ApJ, 525, 886

Arnould, M. 1976, A&A, 46, 117

Arnould, M., & Goriely, S. 2006, Nucl. Phys. A, 777, 157

Audouze, J., & Truran, J. W. 1975, ApJ, 202, 204

Bao, Z. Y., Beer, H., Käppeler, F., Voss, F., Wisshak, K., & Rauscher, T. 2000, At. Data Nucl. Data Tables, 76, 70

Beer, H., Voss, F., & Winters, R. R. 1992, ApJS, 80, 403

Beer, H., & Ward, R. A. 1981, Nature, 291, 308

Bisterzo, S., Gallino, R., Straniero, O., Cristallo, S., & Käppeler, F. 2010, MNRAS, 404, 1529

Burbidge, E. M., Burbidge, G. R., Fowler, W. A., & Hoyle, F. 1957, Rev. Mod. Phys., 29, 547

Busso, M., Gallino, R., Lambert, D. L., Travaglio, C., & Smith, V. V. 2001, ApJ, 557, 802

Cameron, A. G. W. 1957, AJ, 62, 9

Chamulak, D. A., Brown, E. F., Timmes, F. X., & Dupczak, K. 2008, ApJ, 677, 160

Cheoun, M.-K., Ha, E., Hayakawa, T., Kajino, T., & Chiba, S. 2010, Phys. Rev. C, 82, 035504

Contardo, G., Leibundgut, B., & Vacca, W. D. 2000, A&A, 359, 876

Cristallo, S., Straniero, O., Gallino, R., Piersanti, L., Domínguez, I., & Lederer, M. T. 2009, ApJ, 696, 797

Denissenkov, P. A., & Tout, C. A. 2003, MNRAS, 340, 722

Dillmann, I., Heil, M., Käppeler, F., Plag, R., Rauscher, T., & Thielemann, F.-K. 2006, in AIP Conf. Proc. 819, KADoNiS—The Karlsruhe Astrophysical Database of Nucleosynthesis in Stars, ed. A. Woehr & A. Aprahamian (Melville, NY: AIP), 123

Dillmann, I., Käppeler, F., Rauscher, T., Thielemann, F.-K., Gallino, R., & Bisterzo, S. 2008a, Nuclei in the Cosmos X, POS 091

Dillmann, I., Rauscher, T., Heil, M., Käppeler, F., Rapp, W., & Thielemann, F.-K. 2008b, J. Phys. G: Nucl. Part. Phys., 35, 014029

Domínguez, I., Höflich, P., & Straniero, O. 2001, ApJ, 557, 279

Farouqi, K., Kratz, K.-L., & Pfeiffer, B. 2009, PASA, 26, 194

Fink, M., Röpke, F. K., Hillebrandt, W., Seitenzahl, I. R., Sim, S. A., & Kromer, M. 2010, A&A, 514, 53

Fisher, T., Whitehouse, S. C., Mezzacappa, A., Thielemann, F.-K., & Liebendöfer, M. 2010, A&A, 517, A80

Fisker, J. L., Hoffman, R. D., & Pruet, J. 2009, ApJ, 690, L135

Frölich, C., et al. 2006, ApJ, 637, 415

Fujimoto, S.-I., Hashimoto, M.-A., Koike, O., Arai, K., & Matsuba, R. 2003, Nucl. Phys. A, 718, 611

Fujimoto, S.-I., Hashimoto, M.-A., Kotake, K., & Yamada, S. 2007, ApJ, 656, 382

Gallino, R., Arlandini, C., Busso, M., Lugaro, M., Travaglio, C., Straniero, O., Chieffi, A., & Limongi, M. 1998, ApJ, 497, 388

Goriely, S., García-Senz, D., Bravo, E., & José, J. 2005, A&A, 444, L1

Goriely, S., José, J., Hernanz, M., Rayet, M., & Arnould, M. 2002, A&A, 383, L27

Goriely, S., & Mowlawi, N. 2000, A&A, 362, 599

Hayakawa, T., Iwamoto, M., Kajino, T., Shizuma, T., Umeda, H., & Nomoto, K. 2006, ApJ, 648, L47

Hayakawa, T., Iwamoto, M., Kajino, T., Shizuma, T., Umeda, H., & Nomoto, K. 2008, ApJ, 685, 1089

Hayakawa, T., Kajino, T., Chiba, S., & Mathews, G. J. 2010a, Phys. Rev. C, 81, 052801

Hayakawa, T., Kajino, T., Mohr, P., Chiba, S., & Mathews, G. J. 2010b, Phys. Rev. C, 82, 058801

Herwig, F., Blöcker, T., Schönberner, D., & El Eid, M. 1997, A&A, 324, L81

Herwig, F., Lugaro, M., & Langer, N. 2003, ApJ, 593, 1056

Hillebrandt, W., & Niemeyer, J. C. 2000, ARA&A, 38, 191

Hollowell, D. E., & Iben, I., Jr. 1988, ApJ, 333, L25

Howard, W. M., & Meyer, B. S. 1993, in Proc. 2nd International Symposium on Nuclear Astrophysics, Karlsruhe, Germany, ed. F. Käppeler & K. Wisshak (Bristol: Institute of Physics Publishing), 575

Howard, W. M., Meyer, B. S., & Woosley, S. E. 1991, ApJ, 373, L5

Iben, I., Jr. 1981, ApJ, 243, 987

Iben, I., Jr., & Tutukov, A. V. 1991, ApJ, 370, 615

Iwamoto, K., et al. 1999, ApJS, 125, 439

Iwamoto, N., Umeda, H., & Nomoto, K. 2005, in Origin of Matter and Evolution of Galaxies, ed. M. Terasawa et al. (Singapore: World Scientific), 493

Jackson, A. P., Calder, A. C., Townsley, D. M., Chamulak, D. A., Brown, E. F., & Timmes, F. X. 2010, ApJ, 720, 99

Käppeler, F., Gallino, R., Bisterzo, S., & Aoki, W. 2011, Rev. Mod. Phys., 83, 157

Käppeler, F., Arlandini, C., Heil, M., et al. 2004, Phys. Rev. C, 69, 5802

Kasen, D., Röpke, F. K., & Woosley, S. E. 2009, Nature, 460, 869

Khokhlov, M. A. 1991, A&A, 246, 383

Kusakabe, M., Iwamoto, N., & Nomoto, K. 2005, Nucl. Phys. A, 758, 459

Kusakabe, M., Iwamoto, N., & Nomoto, K. 2011, ApJ, 726, 25

Langanke, K., & Martínez-Pinedo, G. 2000, Nucl. Phys. A, 673, 481

Langer, N., Heger, A., Wellstein, S., & Herwig, F. 1999, A&A, 346, L37

Li, W., et al. 2011, MNRAS, 412, 1441

Maeda, K., Röpke, F. K., Fink, M., Hillebrandt, W., Travaglio, C., & Thielemann, F.-K. 2010, ApJ, 712, 624

Marrone, S., et al. 2006, Phys. Rev. C, 73, 034604

Mazzali, P. A., Röpke, F. K., Benetti, S., & Hillebrandt, W. 2007, Science, 315, 825

Mohr, P., Käppeler, F., & Gallino, R. 2007, Phys. Rev. C, 75, 012802

Nagataki, S., Hashimoto, N. A., Sato, K., & Yamada, S. 1997, ApJ, 486, 1026

Nemeth, Z., Käppeler, F., Theis, C., Belgya, T., & Yates, S. W. 1994, ApJ, 426, 357

Nishimura, S., Kotake, K., Hashimoto, M., Yamada, S., Nishimura, N., Fujimoto, S., & Sato, K. 2006, ApJ, 642, 410

Nomoto, K. 1982a, ApJ, 253, 798

Nomoto, K. 1982b, ApJ, 257, 780

Nomoto, K., Thielemann, F.-K., & Yokoi, K. 1984, ApJ, 286, 644

Phillips, M. M., et al. 2007, PASP, 119, 360

Piro, A. L., & Bildsten, L. 2008, ApJ, 673, 1009

Piro, A. L., & Chang, P. 2008, ApJ, 678, 1158

Pruet, J., Hoffman, R. D., Woosley, S. E., Janka, H.-T., & Buras, R. 2006, ApJ, 644, 1028

Rauscher, T., Heger, A., Hoffmann, R. D., & Woosley, S. E. 2002, ApJ, 576, 323

Rauscher, T., & Thielemann, F.-K. 2000, At. Data Nucl. Data Tables, 75, 1

Rayet, M., Arnould, M., Hashimoto, M., Prantzos, N., & Nomoto, K. 1995, A&A, 298, 517

Rayet, M., Arnould, M., & Prantzos, N. 1990, A&A, 227, 271

Reinecke, M., Hillebrandt, W., & Niemeyer, J. C. 1999, A&A, 347, 724

Roberts, L. F., Woosley, S. E., & Hoffman, R. D. 2010, ApJ, 722, 954

Röpke, F. K. 2005, A&A, 432, 969

Röpke, F. K. 2007, ApJ, 668, 1103

Röpke, F. K., & Hillebrandt, W. 2005, A&A, 431, 635

Röpke, F. K., Hillebrandt, W., Niemeyer, J. C., & Woosley, S. E. 2006, A&A, 448, 1

Röpke, F. K., Hillebrandt, W., Schmidt, W., Niemeyer, J. C., Blinnikov, S. I., & Mazzali, P. A. 2007, ApJ, 668, 1132

Röpke, F. K., & Niemeyer, J. C. 2007, A&A, 464, 683

Röpke, F. K., & Schmidt, W. 2009, in Interdisciplinary Aspects of Turbulence, ed. W. Hillebrandt & F. Kupka (Lecture Notes in Physics, Vol. 756; Berlin: Springer), 255

Schatz, H., et al. 2001, Nucl. Phys. A, 688, 150

Seitenzahl, I. R., Röpke, F. K., Fink, M., & Pakmor, R. 2010, MNRAS, 407, 229

Sim, S. A., Röpke, F. K., Hillebrandt, W., Kromer, M., Pakmor, R., Fink, M., Ruiter, A. J., & Seitenzahl, I. R. 2010, ApJ, 714, L52

Straniero, O., Gallino, R., & Cristallo, S. 2006, Nucl. Phys. A, 777, 311

Stritzinger, M., Mazzali, P. A., Sollerman, J., & Benetti, S. 2006, A&A, 460, 793

Sugimoto, D., & Fujimoto, M. Y. 1978, PASJ, 30, 467

Takahashi, K., & Yokoi, K. 1987, At. Data Nucl. Data Tables, 36, 375

The, L.-S., El Eid, M. F., & Meyer, B. S. 2007, ApJ, 655, 1058

Theis, Ch., Käppeler, F., Wisshak, K., & Voss, F. 1998, ApJ, 500, 1039

Thielemann, F.-K., Nomoto, K., & Hashimoto, M. 1996, ApJ, 460, 408

Travaglio, C., Hillebrandt, W., & Reinecke, M. 2005, A&A, 443, 1007

Travaglio, C., Hillebrandt, W., Reinecke, M., & Thielemann, F.-K. 2004, A&A, 425, 1029

Ulrich, R. K. 1973, in Explosive Nucleosynthesis, ed. D. N. Schramm & W. D. Arnett (Austin, TX: Univ. Texas Press), 139

Wanajo, S. 2006, ApJ, 647, 1323

Wanajo, S., Janka, H.-T., & Kubono, S. 2011a, ApJ, 729, 46

Wanajo, S., Janka, H.-T., & Müller, B. 2011b, ApJ, 726, L15

Woosley, S. E. 2007, ApJ, 668, 1109

Woosley, S. E., Hartmann, D. H., Hoffmann, R. D., & Haxton, W. C. 1990, ApJ, 356, 272

Woosley, S. E., & Heger, A. 2007, Phys. Rep., 442, 269

Woosley, S. E., & Howard, W. M. 1978, ApJS, 36, 285

Woosley, S. E., & Howard, W. M. 1990, ApJ, 354, L21

Woosley, S. E., & Kasen, D. 2011, ApJ, 734, 38

Woosley, S. E., Kerstein, A. R., Sankaran, V., Aspden, A. J., & Röpke, F. K. 2009, ApJ, 704, 255

Yokoi, K., & Takahashi, K. 1983, Nature, 305, 198